UC Riverside

UC Riverside Electronic Theses and Dissertations

Title

Processing-Structure-Property Relationships in Heterogeneously Structured Metals

Permalink

Author

Shahrezaei, Sina

Publication Date

2019

UNIVERSITY OF CALIFORNIA
RIVERSIDE

Processing-Structure-Property Relationships in Heterogeneously Structured Metals

A Dissertation submitted in partial satisfaction
of the requirements for the degree of

Doctor of Philosophy

in

Materials Science and Engineering

by

Sina Shahrezaei

March 2019

Dissertation Committee:
  Dr. Suveen N. Mathaudhu, Chairperson
  Dr. Peter A. Greaney
  Dr. David Kisailus

The Dissertation of Sina Shahrezaei is approved:

_____

_____

_____

Committee Chairperson

University of California, Riverside

Acknowledgments

This dissertation is dedicated to my parents and siblings for their love and support, and

to the love of my life, Felicia.

ABSTRACT OF THE DISSERTATION

Processing-Structure-Property Relationships in Heterogeneously Structured Metals

by

Sina Shahrezaei

Doctor of Philosophy, Graduate Program in Materials Science and Engineering
University of California, Riverside, March 2019
Dr. Suveen N. Mathaudhu, Chairperson

Classical processing of metallic materials is incorporated to selectively improve desired properties by processing that results in a homogenous microstructure; however, the improvement in one property often results in deterioration of another property. For example, the strengths of metals can be increased by grain refinement processing techniques due to grain boundary strengthening (i.e., the Hall-Petch relationship), but a significant loss of ductility is often observed to limit the applicability of these processing methods. To avoid these shortcomings, novel processing techniques are investigated to synthesize metals with spatial heterogeneity in their microstructure. The heterogeneous structure allows combinations of material properties that are not achievable by standalone homogenous counterparts. In this dissertation, I have investigated two different processing techniques for the formation of heterogeneously structured metals and explored their structure-property relationship.

Surface severe plastic deformation (S2PD) techniques such as surface mechanical attrition treatment (SMAT) allow processing of metals to form a gradient of stored deformation and microstructure to increase strengths and retain ductility. Herein, SMAT

of Cu followed by annealing at temperatures of 175 °C, 225 °C, and 275 °C for one hour is performed to investigate the mechanical properties-microstructure evolution. Following the annealing, the microstructural evaluation revealed a recrystallized layer near the treated surface that grew in depth with an increase in temperature. A substantial increase in uniform elongation was observed after annealing at 225 °C and 275 °C. The results indicate the importance of a deformation-free microstructure in ductility of the S2PD processed metals.

Bulk metallic glasses (BMG) are best known for their high strength; however, due to their limited tensile plasticity, they are undesirable for most structural applications. Nanolaminated amorphous/crystalline metallic composites fabricated via deposition techniques have been shown to deform homogeneously while demonstrating extraordinary mechanical properties including high strength and ductility. However, their fabrication is limited in size and scalability potential. Herein, accumulative roll bonding (ARB) has been demonstrated as a scalable fabrication technique for the processing of nanolaminated Zr-based BMG/Ni composites. Refined BMG layers with thicknesses as small as 34 nm and an amorphous/crystalline interface with an effective interface width of 3-4nm have been characterized.

TABLE OF CONTENTS

List of Figures

List of Tables

Chapter 1: Introduction

1.1 Overview

Heterogeneously structured metals are defined as metals that have a spatial variation in microstructure and are not necessarily single-phased. Contrary to heterogeneous structures, a homogenously-structured metal consists of microstructural features that do not vary significantly with distance in an observable and quantifiable manner. In a homogenous metal, the properties such as mechanical, wear, corrosion, and electrical vary as a function of the microstructural features (e.g. grain size, stored deformation, texture, etc.); for example, by reducing the grain size, due to grain boundary strengthening (i.e. the Hall-Petch relationship) the yield strength of the metal increases (for grain sizes smaller than 10nm an inverse Hall-Petch relationship is often observed) [1]. Heterogeneously-structured metals can be beneficial by a combination of properties from individual microstructural components that may not be possible by the standalone homogenous counterparts [2]; therefore, heterogeneous structured metals can increase the property space by allowing a broadened possibility of microstructure and properties combinations.

In this dissertation, three different heterostructures are studies. The first heterostructure is formed by a process called surface severe plastic deformation (S2PD) which forms a gradient of microstructure starting from the treated surface. The second heterostructure type is made by annealing S2PD processed materials so that a portion of the gradient region is replaced by deformation-free recrystallized grains in order to investigate the role of deformation-free recrystallized microstructure on the strength and

ductility of S2PD processed materials. The third type of heterostructure is obtained by accumulative roll bonding (ARB) process of a Zr-based bulk metallic glass (BMG) and Ni to develop a processing technique for formation of laminated amorphous/crystalline (a/c) with a potential for superior ductility.

1.2 Surface Severe Plastic Deformation (S2PD)

S2PD processing techniques have recently been incorporated in a variety of materials to create a heterogeneous structure consisting of a gradient of grain size starting from ultra-fine or nanocrystalline grain from the surface to coarse-grain in the core [8–10]. The gradient structures formed by S2PD processing techniques are known to improve properties such as strengths and fatigue life while often maintaining a high tensile ductility [9–13]. The gradient layer accommodates strength while the deformation-free coarse-grained core is attributed to higher mechanical stability and retention of ductility. A few common S2PD processing methods are surface mechanical attrition treatment (SMAT) [10], surface mechanical grinding treatment (SMGT) [8], and ultrasonic shot peening (USSP) [14]. SMAT involves dynamic plastic deformation induced via repeated impacts of balls with high velocity to the surface of a material [15]. The grain refinement mechanism of S2PD processed metals can vary based on stacking fault energy but is hypothesized to be similar to severe plastic deformation (SPD) processes [15].

SPD is a category of metal processing techniques that utilize a large plastic strain to refine the grain size and increase the strengths [3,4]. SPD processes can produce ultra-fine grained (UFG) metals with high strengths while maintaining a constant geometry [3].

The grain refinement mechanism is explained elsewhere [4] and is briefly summarized. At low strains, a high dislocation density is accumulated within the initial microstructure. The high dislocation density within the microstructure recovers into low energetic configurations (i.e., dislocations cells) with small misorientation across their boundaries. Additional strain further increases the misorientation angle and transform the dislocation cells to sub-grains. At high strains, grains with high angle misorientations are formed by further transformation of sub-grains and intersection of microshear bands.

The increase in strength of SPD processed materials is believed to result from grain boundary strengthening according to the Hall-Petch relationship [5,6]. The increase in strength in SPD processed metals often results in a significant reduction in ductility [2,7]. The grains in SPD processed metals are work hardened and the reduction in ductility is likely as a result of a reduction in dislocation storage capacity during uniaxial tension testing [2]. Materials processed by S2PD processes can generate comparable strengths to SPD processes without critical loss of tensile ductility; however, the role of deformation-free coarse-grained microstructure on the ductility of S2PD processed materials has not been investigated elsewhere. Annealing of S2PD processed metals is performed to form a recrystallized deformation-free microstructure near the surface to unravel the role of the deformation-free microstructures on the ductility of S2PD processed metals.

1.3 Accumulative Roll Bonding (ARB)

The third heterostructure that is investigated in this dissertation consists of implementing ARB to fabricate alternating layers of a Zr-based bulk metallic glass

(BMG) and Ni. Roll bonding is a solid-state bonding process between different material sheets to produce one-body solid material. In this process, the expansion of interfacing surfaces causes fracture of the brittle oxide surface layer and the pressure from the rollers allows extrusion of pristine metals through the surface cracks [45]. When opposing extruded pristine materials make contact, they form an atomic bond. This process generally involves degreasing to remove organic contaminants and wire brushing to create a work hardened and brittle surface layer to enhance the extrusion process. Accumulative roll bonding (ARB) is a severe plastic deformation technique (SPD) that was initially used to obtain microstructural refinement [46]. The process involves surface preparation, roll bonding at 50% reduction, cutting, surface preparation, stacking, and repeating the process until the desired strain is obtained [47]. This continuous process can produce ultrafine grain metals with improved strength. This process has also been applied to other material systems to fabricate laminated composites of two materials with maximum refinement in layer thickness in the nanometer range [48].

1.4 Bulk metallic glass (BMG)/metal composites

The third type heterostructure that is investigated contains fabrication of a laminated a/c composite made from Zr-based BMG and Ni layers via ARB. BMGs are amorphous alloys that are characterized by their lack of long-range atomic order as compared to their conventional crystalline metal counterparts. BMGs are known for their high wear resistance, low coefficient of friction, high corrosion resistance, high elastic limit, and strengths approaching theoretical values [17–19]. Comparable to other glass forming materials, BMGs can be shaped to various forms by thermomechanical

processing routes. Owing to a reduction in viscosity of BMGs at their supercooled liquid region (i.e., $\Delta T = (T_X - T_G)$, where T_X is the crystallization temperature and T_G is the glass transition temperature), BMGs can be processed via thermoplastic forming techniques [22]. The thermomechanical processing parameters can be determined from time-temperature-transformation (TTT) diagrams [23]. When BMGs are heated to their supercooled liquid region, the time it takes for nucleation of crystallization decreases with temperature making this process highly sensitive to time and temperature [24]. Here, we have synthesized an a/c laminated composite via the ARB process performed nominally at the T_G of the BMG.

The observed inhomogeneous flow in BMGs has essential implications on properties such as plasticity, strength, and toughness [18]. At low temperatures, BMGs exhibit extraordinary strengths which often outperform their crystalline counterparts [25]. The absence of slip systems in metallic glasses results in lack of dislocation-based work hardening mechanisms which causes the material to be mechanically unstable after yielding; additionally, there is a tendency for work softening upon yielding at highly localized regions called shear bands [18,19]. Shear banding is thought to be the direct consequence of strain softening of a localized region in metallic glasses, which allows continuous local deformation at these softened regions [18,19]. In an unconstrained metallic glass, the shear band can sustain infinite strain, and material fails at those locations [26,27]; however, in constrained loading conditions such as compression of low aspect ratio specimen, after a single shear band operates and matures, the driving force for shear banding decreases below some threshold value and shear band stops [26]. This

process allows activation of further shear bands in the metallic glass structure and therefore higher plasticity. Utilizing the a/c interfaces that are formed by the ARB process, one can geometrically constrain the BMG phase and allow activation of many shear bands.

The process of shear localization introduces size related deformation changes including the width of a shear band and spacing between shear bands [26]. For constrained geometries, shear bands form in consecutive series in sequential increments with a characteristic spacing to accommodate strain; by scaling down the specimen while maintaining the same geometry, the shear banding spacing must decrease for shear bands to accommodate the same deformation [26][28]. The shear displacement of a single shear band is noted to increase with specimen size [28]. At large enough shear displacements, the metallic glass fractures at those shear bands. Schuh et al. calculated the shear band nucleus to have a diameter of the order of 0.5 μm just as it goes critical [29]. For specimens below this thickness limit, homogenous deformation is predicted; therefore, it is possible to engineer metallic glasses with a higher plastic strain to failure utilizing their size-dependent deformation behavior. The proposed ARB process to fabricate a/c composites has the capability to control the thickness of the BMG phase, allowing size-dependent improvements in the plasticity of the BMG phase.

To make metallic glasses more compatible for structural applications and to prevent catastrophic failure, various techniques have been incorporated to enhance plastic strain to failure of metallic glasses. Since limited plastic strain to failure in metallic glasses is attributed to strain localization in a single shear band, research in this area is

directed to constrain the propagation of the main shear band or catalyze the formation of multiple shear bands to increase the plastic flow to failure. There are two main approaches to distribute shear bands. The first one is an intrinsic approach that relates the mechanical properties such as Poisson's ratio, shear modulus and bulk modulus to the propagation of shear bands [26] which are dependent on the specific alloy composition. The second approach is extrinsic in nature and is where heterogenous structures are formed to better distribute shear band propagations [26].

By introducing structural inhomogeneity in metallic glass matrices, stress concentration within the matrices can allow shear band initiation below the global yield point of the matrix and can allow larger plasticity by introducing a large number of shear bands [26,30]. The stress concentration at the shear front in metallic glass matrices can be large enough that it can cleave or plastically deform the secondary phase material [26]. There are many possible ways to create structural heterogeneities in BMGs, and the most investigated techniques are through partial devitrification [31], a formation of secondary dendritic structures during solidification [32] and the formation of a/c composites via powder extrusion [33]. Another approach to constrain the propagation of the main shear band and allow the formation of additional shear bands is by an introduction of structural heterogeneities in the form of laminated composites containing individual alternating layers of a/c constituents [34–37]. However, the investigated techniques involve processing steps such as hot pressing and soldering designed for small scale specimens. One of the shortcomings of the soldering technique is that the structure has low thermal stability of less than 200 °C [35–37], and the problem with hot pressing is that only very

7

low bonding strengths can be achieved [34]. Other techniques to create laminar metallic glass crystalline composites are electroplating [34], physical vapor deposition on substrates [38][39][40] and explosive bonding [41].

A/c nanolaminated structures that are fabricated via the physical vapor deposition techniques have been shown to enhance ductility and strength [42][43]. Kim et al. investigated a nanolaminated a/c composite of CuZr-Cu and found a correlation between the layer thickness and strength with an optimum metallic glass layer thickness of 100 nm [43]. It is thought that below a critical layer thickness, homogeneous flow can be obtained in metallic glasses which can enhance the plastic strain to failure [43][44], however, physical vapor deposition techniques that are used for fabrication of a/c laminated metals are limited in their scalability potential. A scalable processing technique such as ARB can produce laminated a/c composites making BMGs potentially applicable for structural applications.

1.5 Objectives

1) Investigate the influence of annealing on the microstructure-mechanical property evolution of S2PD processed Cu.

2) Synthesize a/c laminated heterostructures using ARB to investigate the role of a/c interfaces on the deformation behavior of BMGs.

1.6 References

[1]   C.S. Pande, K.P. Cooper, Nanomechanics of Hall–Petch relationship in nanocrystalline materials, Prog. Mater. Sci. 54 (2009) 689–706. doi:10.1016/j.pmatsci.2009.03.008.

[2]   E. Ma, T. Zhu, Towards strength–ductility synergy through the design of heterogeneous nanostructures in metals, Mater. Today. 20 (2017) 323–331. doi:10.1016/j.mattod.2017.02.003.

[3]   A. Azushima, R. Kopp, A. Korhonen, D.Y. Yang, F. Micari, G.D. Lahoti, P. Groche, J. Yanagimoto, N. Tsuji, A. Rosochowski, A. Yanagida, Severe plastic deformation (SPD) processes for metals, CIRP Ann. 57 (2008) 716–735. doi:10.1016/j.cirp.2008.09.005.

[4]   T. Sakai, A. Belyakov, R. Kaibyshev, H. Miura, J.J. Jonas, Dynamic and post-dynamic recrystallization under hot, cold and severe plastic deformation conditions, Prog. Mater. Sci. 60 (2014) 130–207. doi:10.1016/j.pmatsci.2013.09.002.

[5]   N. Hansen, Boundary strengthening in undeformed and deformed polycrystals, Mater. Sci. Eng. A. 409 (2005) 39–45. doi:10.1016/j.msea.2005.04.061.

[6]   M. Kato, Hall&ndash;Petch Relationship and Dislocation Model for Deformation of Ultrafine-Grained and Nanocrystalline Metals, Mater. Trans. 55 (2014) 19–24. doi:10.2320/matertrans.MA201310.

[7]   C.C. Koch, D.G. Morris, K. Lu, A. Inoue, Ductility of Nanostructured Materials, MRS Bull. 24 (1999) 54–58. doi:10.1557/S0883769400051551.

[8]   W.L. Li, N.R. Tao, K. Lu, Fabrication of a gradient nano-micro-structured surface layer on bulk copper by means of a surface mechanical grinding treatment, Scr. Mater. 59 (2008) 546–549. doi:10.1016/j.scriptamat.2008.05.003.

[9]   X. Wu, P. Jiang, L. Chen, F. Yuan, Y.T. Zhu, Extraordinary strain hardening by gradient structure, Proc. Natl. Acad. Sci. 111 (2014) 7197–7201. doi:10.1073/pnas.1324069111.

[10]   K. Lu, J. Lu, Nanostructured surface layer on metallic materials induced by surface mechanical attrition treatment, Mater. Sci. Eng. A. 375–377 (2004) 38–45. doi:10.1016/j.msea.2003.10.261.

[11]   T.H. Fang, W.L. Li, N.R. Tao, K. Lu, Revealing Extraordinary Intrinsic Tensile Plasticity in Gradient Nano-Grained Copper, Science (80-.). 331 (2011) 1587–1590. doi:10.1126/science.1200177.

[12]   K. Lu, Making strong nanomaterials ductile with gradients, Science (80-.). 345 (2014) 1455–1456. doi:10.1126/science.1255940.

[13]   K. DAI, L. SHAW, Analysis of fatigue resistance improvements via surface severe plastic deformation, Int. J. Fatigue. 30 (2008) 1398–1408. doi:10.1016/j.ijfatigue.2007.10.010.

[14]   N.. Tao, M.. Sui, J. Lu, K. Lua, Surface nanocrystallization of iron induced by ultrasonic shot peening, Nanostructured Mater. 11 (1999) 433–440. doi:10.1016/S0965-9773(99)00324-4.

[15]   N.R. Tao, J. Lu, K. Lu, Surface Nanocrystallization by Surface Mechanical Attrition Treatment, Mater. Sci. Forum. 579 (2008) 91–108. doi:10.4028/www.scientific.net/MSF.579.91.

[16]   W. Klement, R.H. Willens, P. Duwez, Non-crystalline Structure in Solidified Gold–Silicon Alloys, Nature. 187 (1960) 869–870. doi:10.1038/187869b0.

[17]   W.L. Johnson, Bulk Glass-Forming Metallic Alloys: Science and Technology, MRS Bull. 24 (1999) 42–56. doi:10.1557/S0883769400053252.

[18]   W.L. Johnson, Bulk amorphous metal—An emerging engineering material, JOM. 54 (2002) 40–43. doi:10.1007/BF02822619.

[19]   W.H. Wang, C. Dong, C.H. Shek, Bulk metallic glasses, Mater. Sci. Eng. R Reports. 44 (2004) 45–89. doi:10.1016/j.mser.2004.03.001.

[20]   A.J. Drehman, A.L. Greer, D. Turnbull, Bulk formation of a metallic glass: Pd 40 Ni 40 P 20, Appl. Phys. Lett. 41 (1982) 716–717. doi:10.1063/1.93645.

[21]   H.W. Kui, A.L. Greer, D. Turnbull, Formation of bulk metallic glass by fluxing, Appl. Phys. Lett. 45 (1984) 615–616. doi:10.1063/1.95330.

[22]   Y. Sun, A. Concustell, A.L. Greer, Thermomechanical processing of metallic glasses: extending the range of the glassy state, Nat. Rev. Mater. 1 (2016) 16039. doi:10.1038/natrevmats.2016.39.

[23]   M. Ferry, K.J. Laws, C. White, D.M. Miskovic, K.F. Shamlaye, W. Xu, O. Biletska, Recent developments in ductile bulk metallic glass composites, MRS Commun. 3 (2013) 1–12. doi:10.1557/mrc.2012.32.

[24]   J. Schroers, Processing of Bulk Metallic Glass, Adv. Mater. 22 (2010) 1566–1597. doi:10.1002/adma.200902776.

[25]   M. ASHBY, A. GREER, Metallic glasses as structural materials, Scr. Mater. 54 (2006) 321–326. doi:10.1016/j.scriptamat.2005.09.051.

[26]   C. Schuh, T. Hufnagel, U. Ramamurty, Mechanical behavior of amorphous alloys, Acta Mater. 55 (2007) 4067–4109. doi:10.1016/j.actamat.2007.01.052.

[27]   A.. Argon, Plastic deformation in metallic glasses, Acta Metall. 27 (1979) 47–58. doi:10.1016/0001-6160(79)90055-5.

[28] R.D. Conner, W.L. Johnson, N.E. Paton, W.D. Nix, Shear bands and cracking of metallic glass plates in bending, J. Appl. Phys. 94 (2003) 904–911. doi:10.1063/1.1582555.

[29] C.A. Schuh, A.C. Lund, T.G. Nieh, New regime of homogeneous flow in the deformation map of metallic glasses: elevated temperature nanoindentation experiments and mechanistic modeling, Acta Mater. 52 (2004) 5879–5891. doi:10.1016/j.actamat.2004.09.005.

[30] R.T. Ott, F. Sansoz, J.F. Molinari, J. Almer, K.T. Ramesh, T.C. Hufnagel, Micromechanics of deformation of metallic-glass–matrix composites from in situ synchrotron strain measurements and finite element modeling, Acta Mater. 53 (2005) 1883–1893. doi:10.1016/j.actamat.2004.12.037.

[31] C. Fan, C. Li, A. Inoue, V. Haas, Deformation behavior of Zr-based bulk nanocrystalline amorphous alloys, Phys. Rev. B. 61 (2000) R3761–R3763. doi:10.1103/PhysRevB.61.R3761.

[32] D.C. Hofmann, J.-Y. Suh, A. Wiest, G. Duan, M.-L. Lind, M.D. Demetriou, W.L. Johnson, Designing metallic glass matrix composites with high toughness and tensile ductility, Nature. 451 (2008) 1085–1089. doi:10.1038/nature06598.

[33] S.N. Mathaudhu, K. Ted Hartwig, I. Karaman, Consolidation of blended powders by severe plastic deformation to form amorphous metal matrix composites, J. Non. Cryst. Solids. 353 (2007) 185–193. doi:10.1016/j.jnoncrysol.2006.06.009.

[34] A.T. Alpas, J.D. Embury, Flow localization in thin layers of amorphous alloys in laminated composite structures, Scr. Metall. 22 (1988) 265–270. doi:10.1016/S0036-9748(88)80346-6.

[35] Y. Leng, T.H. Courtney, Multiple shear band formation in metallic glasses in composites, J. Mater. Sci. 26 (1991) 588–592. doi:10.1007/BF00588291.

[36] Y. Leng, T.H. Courtney, Some tensile properties of metal-metallic glass laminates, J. Mater. Sci. 24 (1989) 2006–2010. doi:10.1007/BF02385414.

[37] Y. Leng, T.H. Courtney, Fracture behavior of laminated metal-metallic glass composites, Metall. Trans. A. 21 (1990) 2159–2168. doi:10.1007/BF02647877.

[38] M.C. Liu, J.C. Huang, H.S. Chou, Y.H. Lai, C.J. Lee, T.G. Nieh, A nanoscaled underlayer confinement approach for achieving extraordinarily plastic amorphous thin film, Scr. Mater. 61 (2009) 840–843. doi:10.1016/j.scriptamat.2009.07.010.

[39] M.C. Liu, C.J. Lee, Y.H. Lai, J.C. Huang, Microscale deformation behavior of amorphous/nanocrystalline multilayered pillars, Thin Solid Films. 518 (2010) 7295–7299. doi:10.1016/j.tsf.2010.04.096.

[40] M.C. Liu, X.H. Du, I.C. Lin, H.J. Pei, J.C. Huang, Superplastic-like deformation in metallic amorphous/crystalline nanolayered micropillars, Intermetallics. 30 (2012) 30–34. doi:10.1016/j.intermet.2012.03.037.

[41] K.X. Liu, W.D. Liu, J.T. Wang, H.H. Yan, X.J. Li, Y.J. Huang, X.S. Wei, J. Shen, Atomic-scale bonding of bulk metallic glass to crystalline aluminum, Appl. Phys. Lett. 93 (2008) 081918. doi:10.1063/1.2976667.

[42] Y. Wang, J. Li, A. V. Hamza, T.W. Barbee, Ductile crystalline-amorphous nanolaminates, Proc. Natl. Acad. Sci. 104 (2007) 11155–11160. doi:10.1073/pnas.0702344104.

[43] J.-Y. Kim, D. Jang, J.R. Greer, Nanolaminates Utilizing Size-Dependent Homogeneous Plasticity of Metallic Glasses, Adv. Funct. Mater. 21 (2011) 4550–4554. doi:10.1002/adfm.201101164.

[44] D. Jang, J.R. Greer, Transition from a strong-yet-brittle to a stronger-and-ductile state by size reduction of metallic glasses, Nat. Mater. 9 (2010) 215–219. doi:10.1038/nmat2622.

[45] R. Jamaati, M.R. Toroghinejad, Cold roll bonding bond strengths: review, Mater. Sci. Technol. 27 (2011) 1101–1108. doi:10.1179/026708310X12815992418256.

[46] Y. Saito, H. Utsunomiya, N. Tsuji, T. Sakai, Novel ultra-high straining process for bulk materials—development of the accumulative roll-bonding (ARB) process, Acta Mater. 47 (1999) 579–583. doi:10.1016/S1359-6454(98)00365-6.

[47] N. Tsuji, Y. Saito, S.-H. Lee, Y. Minamino, ARB (Accumulative Roll-Bonding) and other new Techniques to Produce Bulk Ultrafine Grained Materials, Adv. Eng. Mater. 5 (2003) 338–344. doi:10.1002/adem.200310077.

[48] I.J. Beyerlein, J.R. Mayeur, S. Zheng, N.A. Mara, J. Wang, A. Misra, Emergence of stable interfaces under extreme plastic deformation, Proc. Natl. Acad. Sci. 111 (2014) 4386–4390. doi:10.1073/pnas.1319436111.

Chapter 2: Strength-Ductility Modulation Via Surface Severe Plastic Deformation and Annealing

2.1 Introduction

Single-phase heterogeneously-structured metals have offered unique combinations of properties that may not be achievable by homogeneous counterparts. Specifically, the strength-ductility trade-offs that exist in homogeneous ultrafine-grained (UFG) and nanocrystalline (NC) grained metals can be mitigated by the formation of a grain size gradient at the surface [1–4]. This grain size variation has been experimentally shown to facilitate improved retention of ductility in uniaxial tension while achieving high strengths [1–4].

There are different approaches and processing techniques for the formation of heterogeneously structured metals. Two main processing routes for making single-phase heterogeneously-structured metals with large differences in grain size are severe plastic deformation (SPD) followed by annealing [1,4], and surface severe plastic deformation (S2PD) [2,3,5,6]. SPD techniques followed by short annealing treatment offer a bimodal distribution of hard nanocrystalline and soft micrometer-sized recrystallized grains [4]. This bimodal grain distribution has been postulated to offer a strength-ductility synergy due to additional storage of dislocations in recrystallized grains during the mechanical testing. Surface severe plastic deformation (S2PD) processing techniques have recently been incorporated in a variety of materials to fabricate a gradient of grain sizes starting from UFG or NC at the surface to non-deformed coarse grains in the core [3,5,7–9]. A few common examples of the processing methods to induce S2PD are surface mechanical

attrition treatment (SMAT) [2,3,6,10,11], surface mechanical grinding treatment (SMGT) [5], and ultrasonic shot peening (USSP) [7]. The gradient structure (GS) formed by S2PD is shown to improve mechanical properties including strength, fatigue life and wear resistance while maintaining high tensile ductility [3,6,11–13]. The process of SMAT involves dynamic plastic deformation-induced via repeated impacts of high-velocity balls with the surface [14]. The grain refinement mechanism of SMATed metals can vary based on the stacking fault energy of the metal. However, it is mostly attributed to dislocation activity, mechanical twinning and the interaction of mechanical twinning with dislocations [14]. Improvement in ductility of S2PD processed metals has been often considered to be related to strain gradient plasticity [11] and the formation of multiaxial stress-states [2]. In the latter studies, the increase in ductility is assumed to be the result of the gradient structure; however, conditions of the microstructure components forming the gradient and their effects on the overall mechanical properties have received less attention. Particularly, the role of the deformation-free coarse-grained region on the overall ductility of S2PD processed materials has not been explored.

Annealing is most frequently performed to make a work-hardened metal more ductile so it can withstand additional work. During the annealing process, recovery, recrystallization and grain growth can occur which soften the metal by removing the stored strain energy. Static recrystallization transforms the heavily-worked microstructure into a dislocation-free microstructure that can then store a large number of dislocations. This additional dislocation storage capacity permits a higher overall work hardening rate and ductility. Recrystallization temperature is sensitive to the degree of cold work that the

material has experienced [15]; therefore, in S2PD processed metals, recrystallization is expected to occur heterogeneously near the treated surfaces that endured higher plastic deformation, permitting formation of complex heterogeneously-structured metals. Moreover, conclusive information regarding microstructure and mechanical property evolution of S2PD processed single-phased metals during subsequent heat treatment is currently lacking.

Herein, a novel method for creating heterogeneously-structured metals by S2PD followed by selective recrystallization of the produced gradient microstructures is investigated. This approach allows microstructural modifications in a unique way to potentially modulate strength and ductility. Oxygen free high conductivity (OFHC) Cu is processed using the SMAT process, and annealing is performed between 175°C-275°C for one hour to selectively recrystallize part of the microstructure. The role of deformation-free coarse grains in SMAT processed Cu is explored, and the strength-ductility evolution as a function of annealing temperature is evaluated with correlation to microstructural evolution. The results indicate that inducing selective recrystallization via annealing after S2PD processing has the potential to further tailor and improve the mechanical properties of the processed metals.

2.2 Methods

This study is carried out using oxygen-free high conductivity Cu plates with 99.99% purity meeting ASTM F68 (McMaster-Carr). Disks with a diameter of 42mm and initial thicknesses of 6.3 mm and 3 mm are sectioned using electric discharge machining (EDM). The disks are heated at 700 °C for two hours in Ar atmosphere to ensure a

deformation-free, coarse-grained microstructure. The surfaces of the disks are mechanically ground with SiC sandpapers down to 1200 grit to obtain a mirror finish. The SMAT process is carried out using a SPEX Mill 8000D [2,10,16] and is performed by exchanging the lid of the stainless steel SPEX vial with the prepared Cu disk. The Cu disks are processed for 60 minutes on each side using eight 440C steel balls with 8mm diameter at room temperature. To ensure that the SMAT process is performed near room temperature, the vial and the disk are periodically cooled in air to limit temperature rise. The thicknesses of the Cu disks are reduced by the SMAT process from 6.3 mm and 3 mm to nominally 5.3 mm and 2.2 mm, respectively. The 5.3 mm SMATed disks were used for cross-section microstructural characterizations and microhardness, while the 2.2mm SMATed disks were used for tension test and post-tension microhardness measurements. The processed disks are sectioned through-thickness using a lubricated diamond saw to minimize microstructural changes during the sectioning process. Specimens are annealed under Ar atmosphere for 60 minutes at temperatures of 175 °C, 225 °C, and 275 °C and cooled inside the furnace. For cross-sectional microstructural characterizations, the specimens are first ground using conventional metallurgical specimen preparation techniques and then electropolished using the technique reported by Zhang et al. [17]. A Phase II Vickers microhardness tester is used for cross-sectional hardness measurement with a 10 grams load and 15 seconds dwell time. Backscattered electron scanning electron microscope (BSE-SEM) imaging is performed on an FEI NNS450 SEM using a concentric backscattered detector (CBS) at 5 KV, which improves electron channeling contrast. Tension testing is done on a universal mechanical tester

from TestResources using an Epsilon axial extensometer model 3542 (12.7 mm gauge length) at a nominal strain rate of $1.3 \times 10^{-4} \; s^{-1}$ for the coarse-grained, SMATed, and annealed SMATed specimens. Tension test specimens with width of 3 mm and gage length of 12.7 mm and thicknesses of 2.2 mm (SMATed and heat treated SMATed specimens) and 3 mm (coarse grain specimen) that are modified from ASTM E8/E8M − 15a are cut from the processed disks using EDM. Cross-sectional Electron Backscatter Diffraction (EBSD) analysis is performed using an Oxford EBSD detector installed in a FEI Nova NanoSEM 450 SEM. The EBSD maps are analyzed via commercial Oxford Tango software. Grain size measurements from BSE-SEM micrographs are conducted using the lineal intercept method/Heyn's technique.

2.3 Results

The cross-sectional SEM micrographs of the SMATed Cu at various depths is shown in Figure 2.1. In this case, the contrast variation in the BSE-SEM micrographs arises from electron channeling which is dependent on the crystallographic orientation of grains with respect to the direction of the electron beam. The cross-sectional micrographs reveal S2PD induced grain refinement from the initial coarse-grain size of 50 μm in the annealed condition to UFG size of 370 nm in the top surface region after the SMAT process (Figure 2.1A). The grain size gradually increases to 1.2 μm and 4.5 μm at depths of 75 μm (Figure 2.1B) and 250 μm, respectively (Figure 2.1C) from the treated surface. Large contrast variations within individual grains are seen in Figure 2.1C indicate that the refined grains contain a high density of dislocations and large internal misorientations. In the core region of the specimen, contrast variation is also seen within grains, which

implies that the coarse-grained microstructure is also work-hardened despite the grains are not being refined (Figure 2.1D).
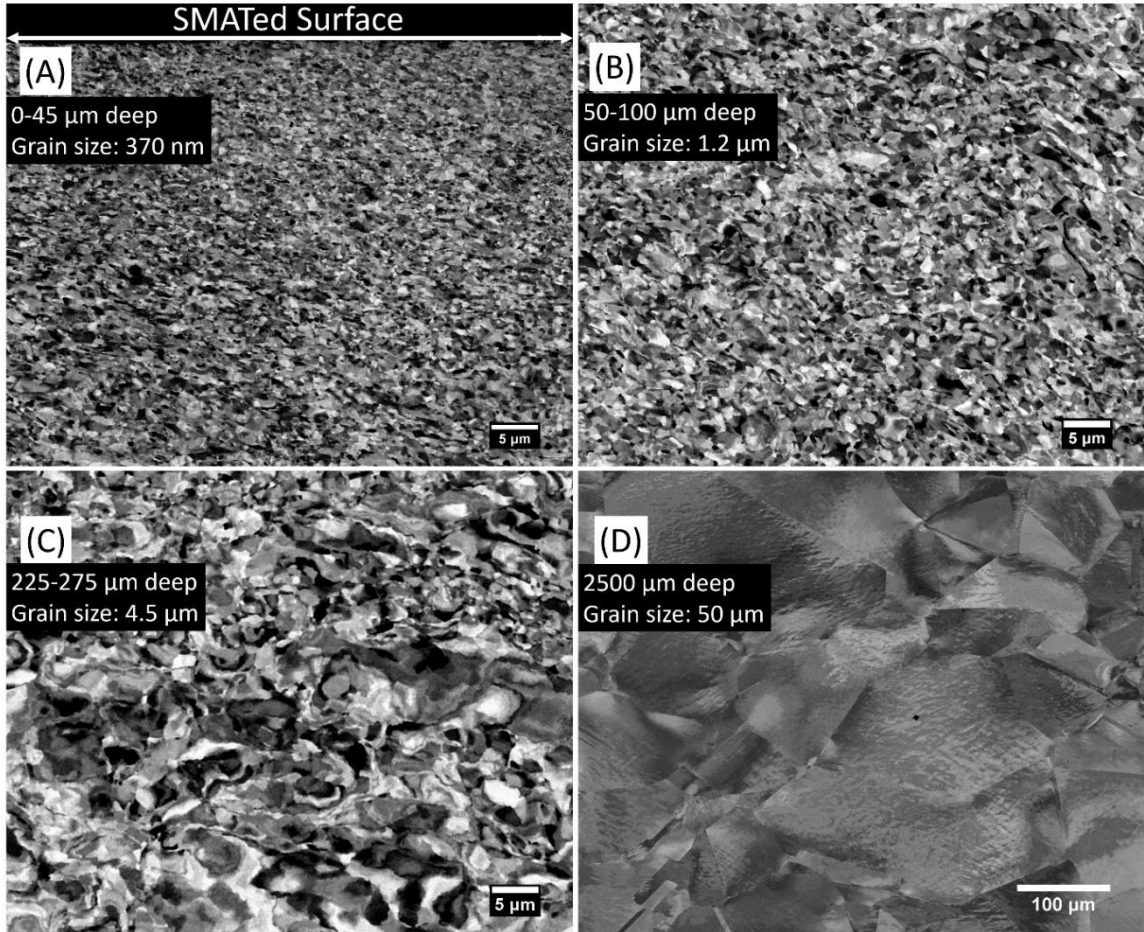
Figure 2.1. Cross-sectional BSE-SEM micrographs. (A) Region from the top treated surface to 45 μm from the treated surface, (B) 50-100 μm from the treated surface, (C) 225-275 μm from the treated surface, and (D) core region, 2500 μm from the treated surface.

The cross-sectional BSE-SEM micrographs of the as-SMATed and post-SMAT annealed Cu specimens are shown in Figure 2.2. The as-SMATed micrograph reveals a gradient in grain size to a depth of 400 μm from the SMATed surface (even though the gradient extends deeper than what is shown in the figure). The resulting gradient microstructure can be divided into three distinct regions: region 1 is the top 50 μm which

has UFG characteristics, region 2 is 50 μm - 275 μm from the treated surface and consists

of grains with gradual increase in size in the range of 1 μm - 5 μm, and in region 3 from
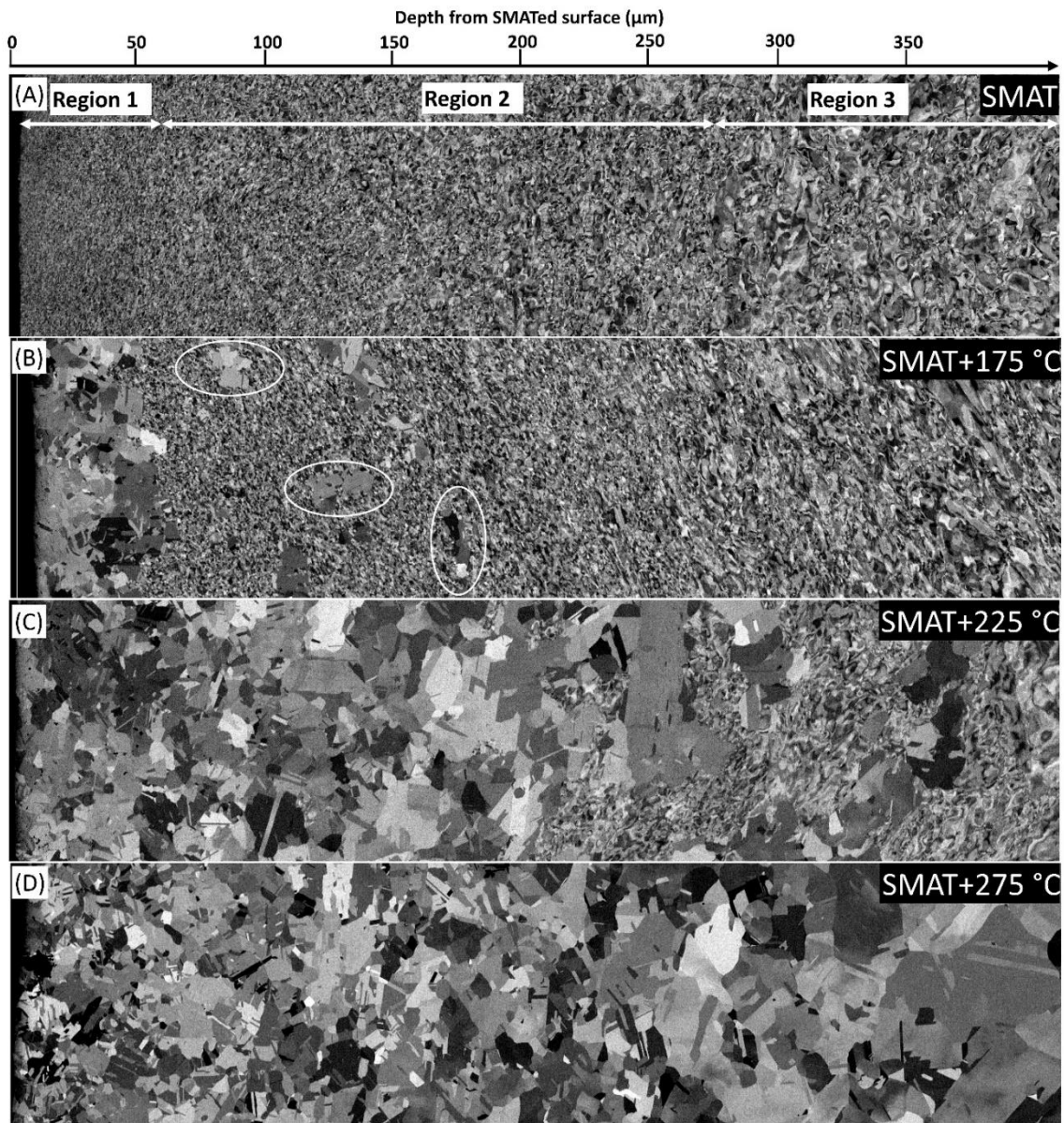
Figure 2.2. Cross-sectional BSE-SEM micrographs of the SMATed and SMAT + annealed for one hour Cu for up to 400 μm from the SMATed surface. (A) As-SMATed Cu, (B) SMATed and annealed at 175 °C with ovals indicating isolated recrystallized grains, (C) SMATed and annealed at 225 °C, and (D) SMATed and annealed at 275 °C.

275 µm to 550 µm (only up to 400 µm is shown here) grains appear to have been refined and a large contrast exists within each grain making grain size estimation difficult (Figure 2.2A). The microstructure of the SMATed and 175 ˚C annealed specimen is shown in Figure 2.2B. Recrystallized grains are visible in the top 50 µm region, and isolated recrystallized grains as deep as 175 µm from the SMATed surface can be seen in Figure 2.2B, and are indicated by the ovals. The 225 ˚C annealed microstructure appears to be recrystallized in the top 200 µm region with isolated recrystallized grains seen as far as 350 µm from the treated surface (Fig 2.2C). The top 550 µm of the SMATed specimen annealed at 275 °C for one hour is recrystallized, and a size gradient of recrystallized grains is visible in Figure 2.2D, with smaller grains toward the surface (only the region 400 µm from the processed surface is shown in this figure).

To correlate the gradient microstructure with the hardness, Vickers microhardness measurement on a cross-section of the as-SMATed and post-SMAT annealed Cu is presented in Figure 2.3. The hardness of the as-SMATed Cu varies with distance away from the treated surface with a maximum hardness of 1.38 ± 0.04 GPa 20 µm from the surface followed by a gradual reduction to 1.04 ± 0.02 GPa at 1100 µm from the surface. Beyond 1100 µm, the hardness remained constant within the measurement error but was higher than that of the strain-relieved initial condition by ~0.3 GPa. It is important to note that both faces of the Cu disk were SMATed and that the increase in hardness in the core region of the specimen is likely due to enhanced work-hardening induced from SMAT processing two sides of a thin disk, which is consistent with the observation in Figure 2.1D. After annealing the specimen at 175 °C, the hardness of the region close to the

SMATed surface reduced to 0.88 ± 0.03 GPa at a depth of 20 µm, and 0.92 ± 0.03 GPa at

a depth of 50 µm. The hardness then follows the same trend as that of the as-SMATed

condition beyond 150 µm, corresponding to the recrystallization depth shown in Figure

2.2B. A similar trend of hardness as a function of distance from the SMATed surface is

found for the specimen annealed at 225 °C which is consistent with the microstructure

seen in Figure 2.2C. The hardness is reduced to 0.88 ± 0.06 GPa at a distance of 200 µm

from the SMATed surface, as observed in the fully-recrystallized region seen in Figure
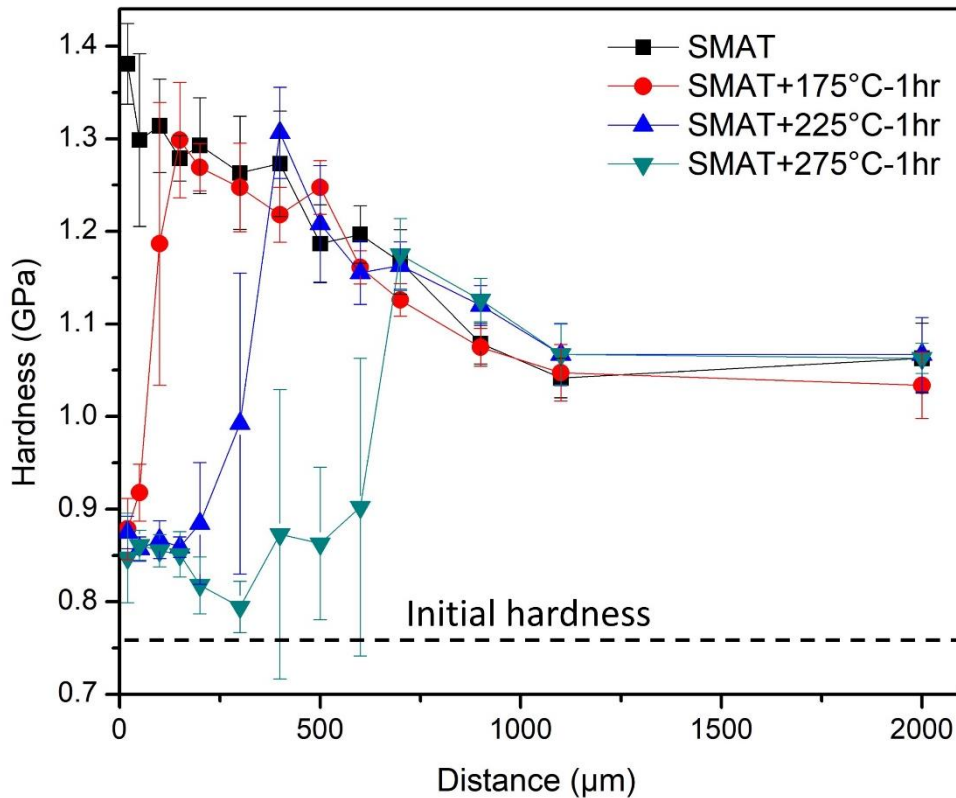
Figure 2.3. Vickers microhardness versus distance from the treated surface for the
samples as-SMATed, SMATed and annealed at 175 °C, SMATed and annealed at
225 °C, and SMAT and annealed at 275 °C conditions.

2.2C. The hardness remains lower than that of the as-SMATed condition up to a distance

of 400 µm. Beyond the depth of 400 µm, the hardness follows the same trend as that of

the as SMATed specimen. For the SMATed Cu annealed at 275 °C, the hardness is reduced to 0.85 ± 0.02 GPa for the first 150 μm followed by further reduction to 0.79 ± 0.03 GPa at 300 μm from the SMATed surface. The low hardness at the 300 μm depth corresponds to the larger recrystallized grains that are seen at a similar depth in Figure 2.3D. The hardness follows the same trend as that of the as-SMATed Cu beyond 700 μm from the as-SMATed surface.

To further probe the relationship between the processed microstructures and the hardness response before and after heat treatment, the cross-sectional EBSD boundary maps for the as-SMATed and SMATed and 225 °C annealed conditions are presented in Figure 2.4. For the as-SMATed condition, the region near the SMATed surface (Figure 2.4A) consists of both high-angle grain boundaries (HAGBs) and low-angle grain boundaries (LAGBs), with the HAGBs occupying a higher fraction of all boundaries but LAGBs, more or less, still existing. At 300-380 μm away from the SMATed surface, the microstructure consists of a much higher fraction of LAGBs, and these are much smaller than grains with HAGBs (Figure 2.4C). After annealing the SMATed Cu at 225 °C, the region near the SMATed surface experiences recrystallization, with the microstructure consisting of annealing twin boundaries and HAGBs and an average grain size of 3.9 μm (Figure 2.4B). The interior of the recrystallized grains appears to be free of deformation as indicated by the lack of LAGBs within those grains (Figure 2.4B). At 300-380 μm from the SMATed surface, the interface between the deformation-free recrystallized and deformed grains is clearly visible (Figure 2.4D); additionally, the unrecrystallized portion of the microstructure after annealing at 225 °C (Figure 2.4D) is very similar to the as-

SMATed microstructure (Figure 2.4C), with both showing pancake-shaped coarse grains

and extensive sub-grain boundaries, in the sense that no observable changes due to
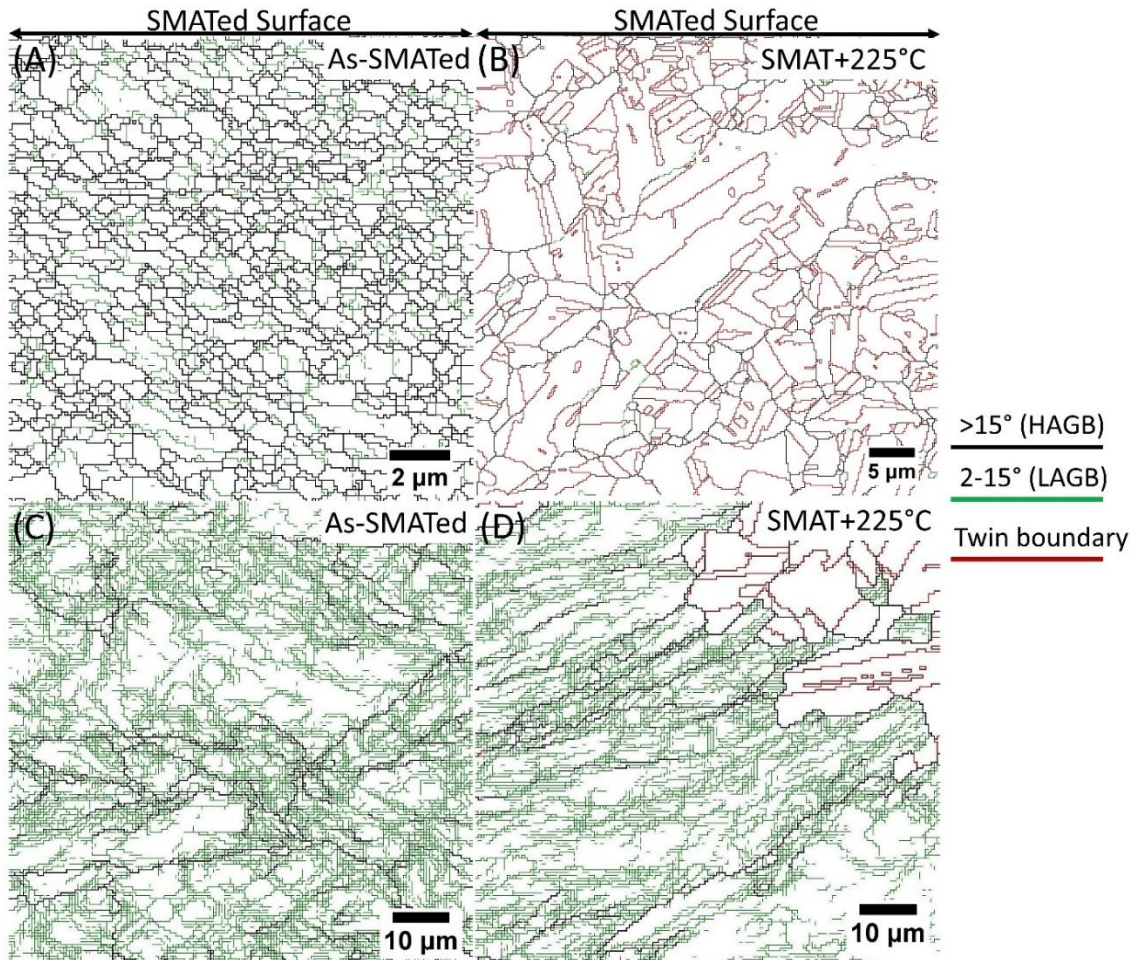
Figure 2.4. Cross-sectional EBSD boundary maps of as-SMATed and SMATed and annealed at 225 °C Cu. (A) Top surface region of the as-SMATed Cu with step size of 100nm, (B) Top surface region of the SMATed and annealed at 225 °C Cu with step size of 200nm, (C) 300-380 μm away from the SMATed surface of the as-SMATed Cu with step size of 500nm, and (D) 300-380 μm away from the SMATed surface of the SMATed and annealed at 225 °C Cu with step size of 500nm.

recovery in that region are visible (the maps were taken at different regions within the

specimen).

To evaluate the mechanical properties of the as-SMATed and SMATed and

annealed Cu, engineering tensile stress-strain curves, as shown in Figure 2.5, are studied.

The mechanical properties are summarized in Table 2.1. After SMAT processing the yield strength (YS) of the Cu is increased by a factor of seven compared with the coarse-grained, strain-relieved condition, while the ultimate tensile strength (UTS) is increased by 45%, however, the necking instability occurred at only 1% uniform elongation (Table
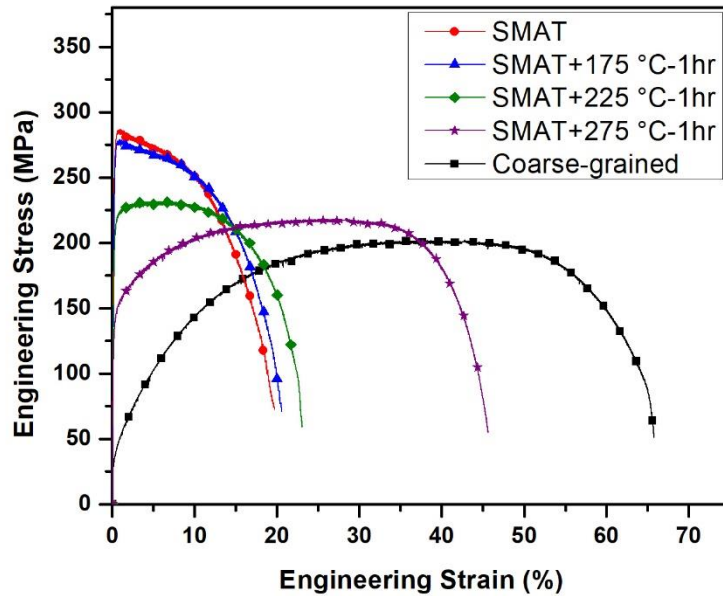
Figure 2.5. Tensile engineering stress-strain curves for the SMATed, SMATed and annealed at 175 °C, 225 °C, 275 °C, and coarse-grained Cu at strain rate of $1.3 \times 10^{-4} \ s^{-1}$

2.1). After annealing the SMATed Cu at 175 °C for one hour, the YS and UTS both decreased by 5% relative to the as-SMATed Cu, while the necking instability was slightly delayed to 1.2%. Increasing the annealing temperature to 225 °C decreased the YS and UTS by 19% and 16% respectively, and the necking instability was significantly delayed to 9%. Annealing the SMATed Cu at 275 °C reduced the YS and UTS by 50% and 25% respectively and necking instability was delayed to 29% elongation, however, with the highest annealing temperature of 275 ˚C, the YS and UTS were still much higher than the coarse-grained condition.

Table 1: Tensile engineering stress-strain data			
Processing condition	Yield strength at 0.2% offset (MPa)	Ultimate tensile strength (MPa)	Uniform elongation (%)
SMATed	276	289	1.0
SMAT + 175 °C	262	275	1.2
SMAT + 225 °C	223	242	9.0
SMAT + 275 °C	138	218	29
Coarse-grained	36	200	42

Cross-sectional Vickers microhardness measurements were performed on the

SMATed, and 225 °C annealed specimen before and after tension testing to understand

the different strain-hardening behavior at regions featuring different grain structures

(Figure 2.6). The recrystallized fraction of the microstructure is approximately 16% for
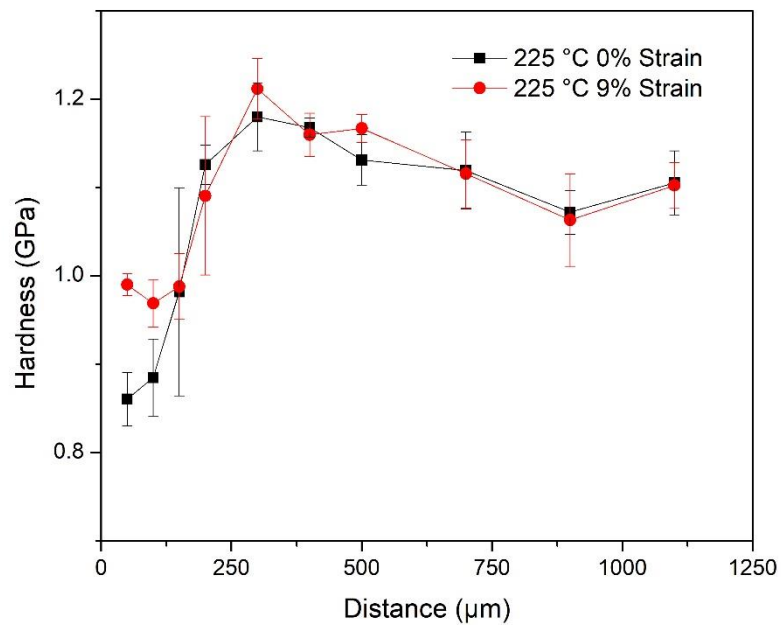
Figure 2.6.   Vickers microhardness versus gradient depth for the SMATed and
annealed at 225 °C Cu before and after 9% uniform elongation.

this specimen. After tension loading, the recrystallized grains on the surface have work-

hardened to a larger degree than the still SMAT-deformed microstructure as evidenced by

a significant increase in hardness at depths of 0-150 μm (Figure 2.4), however, the as-deformed regions do not show a noticeable rise in hardness (within measurement error), indicating minimal working-hardening.

2.4 Discussion

There are two varieties of S2PD processes which are called SMAT by various authors. The first variety uses a high-power ultrasonic head to impact the balls into the surfaces to be treated [6,18,19]. This type of process, in Cu, is reported to induce deformation to a depth of approximately 200 μm [19] in one report and 150 μm [18] in another report (with both using 8mm diameter steel balls), and 110 μm for an interstitial free (IF)-steel (using 4-6mm diameter steel balls) [6]. One distinguishing feature about this process is that the interior region of the treated specimen (i.e., the coarse-grained region) is not work-hardened during the treatment process. It is also important to note that in these reports the initial microstructure of the metal to be processed is fully-recrystallized and has coarse grains. Another S2PD process, which is also called SMAT by various authors including this work, uses a SPEX mixer/mill which is a high-energy ball mill [16][20][10]. For this type of SMAT process, the vial that holds the balls shakes back and forth at approximately 1080 cycles per min allowing the balls to impact the surface of the metal disk to be treated where the metal disk is held stationary at one end of the vial. The resulting deformation depth for this type of SMAT process is approximately 1000 μm for an IF-Steel (SMATed with 12.7 mm diameter steel balls) [16] and approximately 1000 μm for the pure Cu in this work (SMATed with 8 mm diameter steel balls). SMAT processing both sides of the Cu disk, while causing a

gradient of deformation, resulted in appreciable work-hardening in the coarse-grain region of the specimen beyond 1mm from the treated surfaces. Smaller 6.35 mm diameters balls (as opposed to 8 mm diameter balls reported in this work) were implemented, and work hardening of the interior region of the specimen (not shown here) was observed as well. It is, however, speculated that the preservation of the coarse-grained region against work hardening occurs, if even smaller balls or higher thickness specimens are used. Future studies are needed to prove this hypothesis. A possible processing parameter that can cause higher deformation depths in the second variant of the SMAT process is the momentum that is transferred during the inelastic collision of the balls with the surface. Since similar ball sizes and masses are used in the mentioned reports, we speculate that the higher deformation depth in the second variant of SMAT is due to the higher velocity of the balls that impact the surface. The advantage of SMAT using a SPEX mill is that a higher deformation depth allows treatment of materials with much larger cross-sectional areas (assuming constant volume fraction of the treated region) which makes S2PD processes more versatile for various applications.

The overall strengths of the S2PD treated specimen, including both the gradient region and the homogeneous core region, depending on the volume fractions of the two regions, where a higher volume fraction of the gradient region results in higher strengths [19]. The S2PD processed microstructural features such as HAGBs and LAGBs vary with distance from the treated surfaces and prediction of strength needs to be carefully considered. As described by Hansen in 2004 [21], the flow stress of deformed polycrystalline metals requires a modified Hall-Petch relationship taking into

consideration the influence of low angle boundaries. The EBSD maps in Figure 2.4a show that the microstructure of the SMATed Cu consists of low angle and high angle boundaries and that their numbers and relative fractions vary with depth. The strengthening in the top surface region is likely accommodated by a combination and HAGBs and LAGBs; whereas deeper from the treated surface, the higher density of LAGBs should be the main source of strengthening. Therefore, one can assume that the strengthening in the stand-alone gradient region of the S2PD specimen must consider the influence of HAGBs and LAGBs at various depths separately.

Annealing was shown to result in partial recrystallization of the gradient region as a function of temperature, where the recrystallization starts from the treated surface and extends deeper into the gradient structure with an increase in temperature. The stored deformation energy has direct consequences on the thermal stability against recrystallization of the treated layer, which influences both the strength and ductility of the heat-treated specimens. The driving energy for recrystallization is the strain that is stored in the form of dislocations, so a higher dislocation density as result of prior deformation can result in a reduction of the recrystallization temperature [15]. Meanwhile, a smaller initial grain size has been shown to lower the recrystallization temperature [15,22] as well. Therefore, for the gradient region of the SMATed Cu specimen, both the increase in dislocation density and reduction in grain size result in higher propensity to recrystallize as observed in Figure 2.2. This results in a deformation-free recrystallized region near the specimen surface with high dislocation storage capacity. A gradient of grain size is visible in the recrystallized segment of the sample

treated at 275 °C (Figure 2.2D), showing smaller grains toward the surface, and we hypothesize that this change in recrystallized grain size is due to a gradient of recrystallization nucleation sites (nucleation preferentially occurs at HAGBs) which have the highest density near the treated surface.

In this work, the high-volume fraction of the gradient region and the work-hardening of the coarse-grain region has caused the strength of the SMATed Cu to increase by a factor of seven; however, this large increase in strength is accompanied by a significant reduction in uniform tensile elongation. The reduction in uniform elongation after the SMAT process is likely because of the reduction in the overall work-hardening rate $(\frac{d\sigma}{d\varepsilon})$ and the increase in the overall flow stress of the specimen which results in initiation of mechanical instability at lower strains (i.e. $\frac{d\sigma}{d\varepsilon} < \sigma$). As discussed by Rollett and Kocks (1993), work-hardening behavior of metals can be described by four stages [23]. Stage I is only observed in single crystalline metals and is related to dislocation accumulation via dislocation dipole interactions at low strains. Stage II is observed in both single crystalline (with increase in the strain) and polycrystalline (at low strains) metals and is characterized by a high and constant work-hardening rate. The hardening rate in stage II is associated with forest hardening due to the activation of multiple slip systems. At higher strains, stage III of work-hardening is observed, where the work-hardening rate decreases with increases in strain. At the end of stage III, the work-hardening rate transitions to stage IV, as indicated by a small and sustained work-hardening rate which continues to large strains [23]. A reduction in work-hardening rate can occur at stage III and IV because the increase in flow stress can assist constriction

29

processes which allow the combination of two partial dislocations into a screw dislocation, so cross-slip can occur for screw dislocation annihilation [24], therefore increasing the rate of dynamic recovery of dislocations [23]. The SMAT process causes grain refinement and work-hardening of the treated regions, which in turn results in a reduction in work-hardening rate. It has been shown that a pre-strain in different strain paths can cause the skipping of stage III, and direct transition to stage IV with the low work-hardening rates [25]. The SMAT impacted gradient region undergoes a large pre-strain prior to tension testing, so the skipping of stage III within those regions is likley. Moreover, the SMAT treatment in this study also causes work-hardening of the coarse-grained layer which is expected to result in the observed low work-hardening of those regions during the tension test. Therefore, to obtain high ductility, one needs an appropriate fraction of the microstructure to remain deformation free (a recrystallized microstructure). We hypothesize that the overall work-hardening rate of the specimen is generated from individual layers in the treated material and the volume fraction of these layers with specific work-hardening rates will determine the overall work-hardening rate. In other words, assuming that no other phenomenon is occurring due to the interaction of individual layers, the overall work-hardening rate at an instantaneous strain can be determined by the weighted arithmetic mean:

$$\frac{d\sigma}{d\varepsilon} = \frac{\sum_{j=1}^{n} d_j (\frac{d\sigma}{d\varepsilon})_j}{\sum_{j=1}^{n} d_j}, (\varepsilon = \varepsilon_i) \tag{1}$$

Where $(\frac{d\sigma}{d\varepsilon})_j$ is the work-hardening rate of layer j, d_j is the thickness of layer j, n is the number of layers and ε_i is the instantaneous strain. Utilizing equation 1, one can

approximate optimum thickness fraction of the S2PD resulted in layers with different strengths and work-hardening rates. The deformation depth and volume fraction of the gradient region will have direct implications on the work-hardening rate and strength; furthermore, the existence of a large volume fraction of deformation-free coarse-grained microstructures will provide a higher ductility due to their high dislocation storage capacity. Determination of the work-hardening rate as a function of strain for layers with different deformation histories (i.e. distance, from the treated surface) will be the subject of future work.

The resulting deformation-free microstructure after recrystallization of the layers near the treated surfaces has resulted in an increase in ductility as a function of the treatment temperature. The hardness of the recrystallized regions has been reduced because of grain coarsening near the treated surface and the removal of LAGBs in regions farther away from the treated surface (Figure 2.4d). It is important to note that no noticeable return in hardness to the initial values was observed after annealing at different temperatures (Figure 2.3), which means that the work-hardened coarse grain regions survive after annealing. This is likely because Cu has a medium stacking fault energy which minimizes the static recovery through screw dislocation annihilation by cross-slip. Because of these microstructural transformations, one would expect different evolution of the work-hardening rate to occur in the recrystallized layer. After annealing the specimen, the existence of deformation-free recrystallized microstructures has likely increased the overall work-hardening rate of the specimen. The microhardness presented in Figure 2.6 supports this statement, where the recrystallized grains after annealing underwent higher

work-hardening compared with the rest of the microstructure; therefore, improvements in ductility are likely due to a higher sustained work-hardening rate from the recrystallized layer after heat treatment as well as a reduction in the flow stress. During tension testing, the deformation-free recrystallized layer is expected to work-harden starting from stage II. Due to the pre-straining that is imposed by the SMAT process, the as-deformed microstructure within the gradient and the core is expected to work-harden at later stages with reduced work-hardenability. This shows the importance of a deformation-free microstructure component for the overall ductility of the S2PD processed gradient metals since it can delay the onset of mechanical instability. The knowledge of microstructure and mechanical properties evolution as a function of temperature allows one to assess the applicability of S2PD processed materials for applications requiring operations at elevated temperatures, making the S2PD processed materials more predicable for those applications.

2.5 Conclusion

We have evaluated the microstructure, and mechanical property relationship of as-SMATed and annealed SMAT processed Cu. Consideration of both the HAGBs and LAGBs is shown to be an important factor, and underreported factor when analyzing the strengthening effect of an S2PD process. The findings suggest that the recrystallized microstructure portion free of LAGBs is critical in order to obtain a balance between strength and ductility of the processed material. The stored gradient of deformation causes a reduction in the recrystallization temperature of the SMAT treated Cu, catalyzing the formation of a deformation-free, recrystallized layer near the treated

surface that increases in thickness with annealing temperature. The high dislocation storage capacity of the recrystallized layer has increased the ductility of SMATed Cu after annealing with an observed proportional reduction in strength. The resulting microstructure-mechanical property relationships allow better predictability of the S2PD processed material performance in high-temperature environments.

2.6 References

[1]   E. Ma, T. Zhu, Towards strength–ductility synergy through the design of heterogeneous nanostructures in metals, Mater. Today. 20 (2017) 323–331. doi:10.1016/j.mattod.2017.02.003.

[2]   J. Moering, X. Ma, J. Malkin, M. Yang, Y. Zhu, S. Mathaudhu, Synergetic strengthening far beyond rule of mixtures in gradient structured aluminum rod, Scr. Mater. 122 (2016) 106–109. doi:10.1016/j.scriptamat.2016.05.006.

[3]   K. Lu, J. Lu, Nanostructured surface layer on metallic materials induced by surface mechanical attrition treatment, Mater. Sci. Eng. A. 375–377 (2004) 38–45. doi:10.1016/j.msea.2003.10.261.

[4]   Y. Wang, M. Chen, F. Zhou, E. Ma, High tensile ductility in a nanostructured metal, Nature. 419 (2002) 912–915. doi:10.1038/nature01133.

[5]   W.L. Li, N.R. Tao, K. Lu, Fabrication of a gradient nano-micro-structured surface layer on bulk copper by means of a surface mechanical grinding treatment, Scr. Mater. 59 (2008) 546–549. doi:10.1016/j.scriptamat.2008.05.003.

[6]   X. Wu, P. Jiang, L. Chen, F. Yuan, Y.T. Zhu, Extraordinary strain hardening by gradient structure, Proc. Natl. Acad. Sci. 111 (2014) 7197–7201. doi:10.1073/pnas.1324069111.

[7]   N.. Tao, M.. Sui, J. Lu, K. Lua, Surface nanocrystallization of iron induced by ultrasonic shot peening, Nanostructured Mater. 11 (1999) 433–440. doi:10.1016/S0965-9773(99)00324-4.

[8]   K. Wang, N.R. Tao, G. Liu, J. Lu, K. Lu, Plastic strain-induced grain refinement at the nanometer scale in copper, Acta Mater. 54 (2006) 5281–5291. doi:10.1016/j.actamat.2006.07.013.

[9]   A.L. Ortiz, J.W. Tian, J.C. Villegas, L.L. Shaw, P.K. Liaw, Interrogation of the microstructure and residual stress of a nickel-base alloy subjected to surface severe plastic deformation, Acta Mater. 56 (2008) 413–426. doi:10.1016/j.actamat.2007.10.003.

[10]   K.A. Darling, M.A. Tschopp, A.J. Roberts, J.P. Ligda, L.J. Kecskes, Enhancing grain refinement in polycrystalline materials using surface mechanical attrition treatment at cryogenic temperatures, Scr. Mater. 69 (2013) 461–464. doi:10.1016/j.scriptamat.2013.05.036.

[11]   X.L. Wu, P. Jiang, L. Chen, J.F. Zhang, F.P. Yuan, Y.T. Zhu, Synergetic Strengthening by Gradient Structure, Mater. Res. Lett. 2 (2014) 185–191. doi:10.1080/21663831.2014.935821.

[12] T.H. Fang, W.L. Li, N.R. Tao, K. Lu, Revealing Extraordinary Intrinsic Tensile Plasticity in Gradient Nano-Grained Copper, Science (80-.). 331 (2011) 1587–1590. doi:10.1126/science.1200177.

[13] K. Lu, Making strong nanomaterials ductile with gradients, Science (80-.). 345 (2014) 1455–1456. doi:10.1126/science.1255940.

[14] N.R. Tao, J. Lu, K. Lu, Surface Nanocrystallization by Surface Mechanical Attrition Treatment, Mater. Sci. Forum. 579 (2008) 91–108. doi:10.4028/www.scientific.net/MSF.579.91.

[15] J.E. Burke, D. Turnbull, Recrystallization and grain growth, Prog. Met. Phys. 3 (1952) 220–292. doi:10.1016/0502-8205(52)90009-9.

[16] J. Moering, X. Ma, G. Chen, P. Miao, G. Li, G. Qian, S. Mathaudhu, Y. Zhu, The role of shear strain on texture and microstructural gradients in low carbon steel processed by Surface Mechanical Attrition Treatment, Scr. Mater. 108 (2015) 100–103. doi:10.1016/j.scriptamat.2015.06.027.

[17] B. Zhang, W.H. Lee, R. Piner, I. Kholmanov, Y. Wu, H. Li, H. Ji, R.S. Ruoff, Low-Temperature Chemical Vapor Deposition Growth of Graphene from Toluene on Electropolished Copper Foils, ACS Nano. 6 (2012) 2471–2476. doi:10.1021/nn204827h.

[18] Z. Yin, X. Yang, X. Ma, J. Moering, J. Yang, Y. Gong, Y. Zhu, X. Zhu, Strength and ductility of gradient structured copper obtained by surface mechanical attrition treatment, Mater. Des. 105 (2016) 89–95. doi:10.1016/j.matdes.2016.05.015.

[19] X. Yang, X. Ma, J. Moering, H. Zhou, W. Wang, Y. Gong, J. Tao, Y. Zhu, X. Zhu, Influence of gradient structure volume fraction on the mechanical properties of pure copper, Mater. Sci. Eng. A. 645 (2015) 280–285. doi:10.1016/j.msea.2015.08.037.

[20] H. Murdoch, K. Darling, A. Roberts, L. Kecskes, Mechanical Behavior of Ultrafine Gradient Grain Structures Produced via Ambient and Cryogenic Surface Mechanical Attrition Treatment in Iron, Metals (Basel). 5 (2015) 976–985. doi:10.3390/met5020976.

[21] N. Hansen, Hall–Petch relation and boundary strengthening, Scr. Mater. 51 (2004) 801–806. doi:10.1016/j.scriptamat.2004.06.002.

[22] B. Bay, N. Hansen, Initial stages of recrystallization in aluminum of commercial purity, Metall. Trans. A. 10 (1979) 279–288. doi:10.1007/BF02658335.

[23] A.D. Rollett, U.F. Kocks, A Review of the Stages of Work Hardening, Solid State Phenom. 35–36 (1993) 1–18. doi:10.4028/www.scientific.net/SSP.35-36.1.

[24]   G. Lu, V. V. Bulatov, N. Kioussis, Dislocation constriction and cross-slip: An ab initio study, Phys. Rev. B. 66 (2002) 144103. doi:10.1103/PhysRevB.66.144103.

[25]   M. Zandrahimi, S. Platias, D. Frice, D. Barrett, P.S. Bate, W.T. Roberts, Effects of changes in strain path on work hardening in cubic metals, Metall. Trans. A. 20 (1989) 2471–2482. doi:10.1007/BF02666682.

Chapter 3: Synthesis of Amorphous/Crystalline Laminated Metals via Accumulative Roll Bonding

3.1 Introduction

Bulk metallic glasses (BMG) are amorphous alloys that are best characterized by their high strengths, hardness, and wear resistance; however, their structural applications are limited due to their inadequate plastic strain to failure. Under loading, plastic deformation occurs locally at a few shear bands, and the material catastrophically fails by localization of strain at the main shear band [1][2][3]. Under-constrained loading geometries, BMGs can often accommodate higher plastic strain to failure by activation of larger number of shear bands [3][4]. Studies have shown that a minimum critical volume is required for nucleation of shear bands [5][6]. Below that critical dimension, the deformation is accommodated by collective atomic rearrangements known as shear transformation zones (STZ), where homogeneous deformation can take place [6][7]. Indeed, micropillar compression experiments on amorphous $Pd_{77} Si_{23}$, have shown that below a pillar diameter of 400 nm, the deformation is homogenous and shear band formation is prevented [6]. Nano-tension tests of BMGs have indicated a critical thickness below 100 nm which the material deforms in a homogenous manner [7].

Utilization of monolithic materials with this dimension-limited homogenous deformation in standalone BMGs is not applicable for applications that require large sample dimensions. Computational and experimental work has shown that homogenous deformation is possible in amorphous/crystalline (a/c) nanolaminates, where homogenous deformation is accommodated by a collaborative interaction of STZs and dislocations [8]

37

[9][10][11]. Synthesis of a/c nanolaminates is currently only limited to thin film techniques, such as physical vapor deposition (PVD). Thus specimens fabricated with thin-film techniques are limited in size and scalability [9][12]. Mechanical properties of a/c nanolaminates that are synthesized using PVD are measured using micro-pillars and nano-tensile specimens, which may not represent the bulk behavior of the specimen directly; therefore, a scalable synthesis technique is required for formation of a/c nanolaminates for macro-scale mechanical testing and development of other potential applications.

Accumulative roll bonding (ARB) has been proven to be a scalable and inexpensive technique for the synthesis of nanolaminated metals consisting of dissimilar metallic constituents [13][14]. Roll bonding is a solid-state bonding process capable of forming a metallurgical bond between two or more metallic constituents. During the roll bonding process, the contacting surfaces are expanded, the brittle oxide surface layers are cracked, the pristine metals are extruded between the cracks, and once the extruded materials come in contact under high compressive pressure from the rolls, they form a metallurgical bond [15,16]. In the roll bonding process, the material is often rolled to 50% in thickness reduction, which increases the length of the rolled piece to nominally twice from the original; the roll bonded specimen is then cut in half, stacked, and rolled to 50% reduction again. This ARB process is repeated for several cycles to refine the thickness of individual layers to the desired amount. During each cycle of the ARB process, the number of layers is doubled, the thickness of individual layers is reduced to half, and at the same time, the overall thickness of the specimen is maintained.

Here, we propose ARB as a scalable technique for the synthesis of a/c nanolaminated metals. Several attempts to utilize ARB for the synthesis of a/c composites using BMGs as the amorphous material [17,18] have been made; however, the thermo-mechanical processing control has proven challenging due to crystallization and fragmentation of the BMG phase. These problems can be remedied by selection of BMGs with wider processing windows, higher stabilities against crystallization and careful consideration of the processing parameters, such as roll speed, temperature range, and importantly, time at temperature. BMGs can deform homogeneously at their supercooled liquid region (SLR) while experiencing a significant reduction in their flow stress which makes the ARB process possible; SLR is defined as the temperature difference between the onset of crystallization (T_x) and the glass transition temperature (T_g). Crystallization can be avoided by careful consideration of time-temperature-transformation (TTT) diagram of the selected BMG. Further, an appropriate crystalline phase can be selected so that it has a similar flow stress in the SLR, thus maximizing the possibility for uniform layer reductions. A Zr-based BMG known as the Inoue alloy [19] with a wide SLR as the BMG constituent for the ARB process has been used for this study.

In this work, the ARB technique for formation of a/c nanolaminate structured metals has been experimentally evaluated. To assess the resulting microstructural evolution as a function of the thermomechanical history of samples, light microcopy, scanning electron microcopy (SEM), and transmission electron microscopy (TEM) are utilized. High-resolution TEM (HRTEM) is used to investigate the resulting

39

amorphous/crystalline interface layers. Criteria for optimum processing parameter selection and processing challenges are discussed in consideration of the experimental results. The resulting a/c interface structure and its transition from disordered to the ordered structure is discussed. Finally, refinement of the amorphous constituent as small as 34 nm in thickness is obtained, indicating the potential of this processing technique for creation of a/c nanolaminated metals with high strength and ductility. A potential application for this composite is electronic shielding of spacecraft electronics against space radiations which often require a layered structure with alternative low-Z and high-Z materials [20].

3.2 Methods

Annealed 99.99% purity Ni sheets of 0.5mm in thickness were cold rolled to 0.2mm in thickness. Ni was chosen based on prior demonstrations of sufficient uniform co-deformability in the SLR via equal channel angular extrusion [21]. A 0.06mm thick Zr 65 Cu 17.5 Ni 10 Al 7.5 at% (Zr65) foil, a Zr-based BMG with a Tg of 361 °C and crystallization temperature of 466 °C, was fabricated at NASA's Jet Propulsion Laboratory (Pasadena, CA) and used as the BMG constituent [22]. Coupons of Zr65 and Ni with dimensions of 2cm by 6cm were cut using a hand shear cutting tool. To remove organic contaminants, the coupons were places inside a hot acetone bath at 60 °C for five minutes followed by sonication for two minutes. Scratch brushing using a rotary tool and a steel brush were performed on the surfaces of the Ni coupons. The role of scratch brushing is to create a work-hardened and brittle top surface layer, so during the rolling process it fractures and allows extrusion of pristine Ni through the cracks which will

bond with the BMG. After scratch brushing, the coupons are stacked and then spot welded at both ends to hold the foils together during the subsequent rolling process. In this work, two different initial layer arrangements were used, one with six Ni and five Zr65 and another with five Ni and four Z65 stacked in Ni/Zr65/Ni/Zr65…/Ni order. The stacks were heated in an argon atmosphere tube furnace at 420 ℃ at a heating rate of 15℃/min and soaked at that temperature for two minutes before rolling. A heated two-high rolling mill (IRM model 4060) with separating force of 18,000 Kg and a roll diameter of 10 cm was used for the roll bonding process. The roll gap was adjusted for 50% reduction, and the lubrication free rolls were heated to 250 ℃ to reduce heat loss from samples during the rolling process. Using heated tweezers, the specimen was inserted into the rolls with roll surface linear speed of 1.2 m/min, and after rolling they were cooled to room temperature in air. A temperature loss of 20-40 ℃ was measured to occur when taking the samples from the furnace and into the rolls. To perform the next ARB cycle, the rolled sample was cut in half using a mechanical saw, the surface of the samples were degreased using acetone impregnated lint free wipes, scratch brushed, spot welded, preheated and rolled the same way. The roll opening gap, however, had to be reduced after every ARB cycle to accommodate work-hardening of the Ni. The initial layer arrangement with five Ni and four Zr65 proved to be difficult to ARB process past four ARB cycles due to its low overall thickness and work-hardening of Ni, and the process was stopped at four ARB cycles. For initial layer arrangement with six Ni and five Zr65, the ARB process was continued up to six ARB cycles.

For microstructural characterization and cross-sectional microhardness measurements, coupons from the ARB processed samples were cut along the transverse direction (TD) using a lubricated, low-speed diamond saw. After encapsulating the coupons in an epoxy mold, the samples were ground and polished. Light microscopy was used to characterize the overall layer thickness and flow behavior of the composite. Microstructural characterization at higher magnifications was performed using an FEI Nova NanoSEM 450 scanning electron microscope (SEM). An FEI Quanta 3D DualBeam 200i focused ion beam (FIB) was used for TEM sample preparation and ion channeling contrast imaging. A FEI Titan Themis 300 HRTEM was used for high magnification imaging of Zr65/Ni interface. Cross-sectional microhardness of the as-received and ARB processed Zr65 was measured using Phase II Vickers microhardness tester with a 100 g and 15 seconds dwell time. Five indentations were taken for each hardness data point, and the measurements were taken at random places within the specimen.

3.3 Results

To investigate the continuity and layer thickness distribution of the Zr65 in the Ni matrix cross-sectional light micrographs are taken at different ARB cycles (Figure 3.1). As marked in Figure 3.1a, the darker contrast is associated with Zr65 layers while the lighter matrix is the Ni. After the first ARB cycle, the thickness of individual Zr65 layers appears to vary across the microstructure with Zr65 having a maximum thickness of 52 μm and a minimum thickness of 10 μm (the starting thickness of Zr65 was 60 μm) (Figure 3.1a). The Zr65 layers are continuous but appear to have developed necking-like

features. After the second rolling cycle, the Zr65 phase developed necking-like features throughout the structure with Zr65 having a maximum thickness of 45 μm and a minimum thickness of 2 μm (Figure 3.1b). After the fourth rolling cycle, the necked
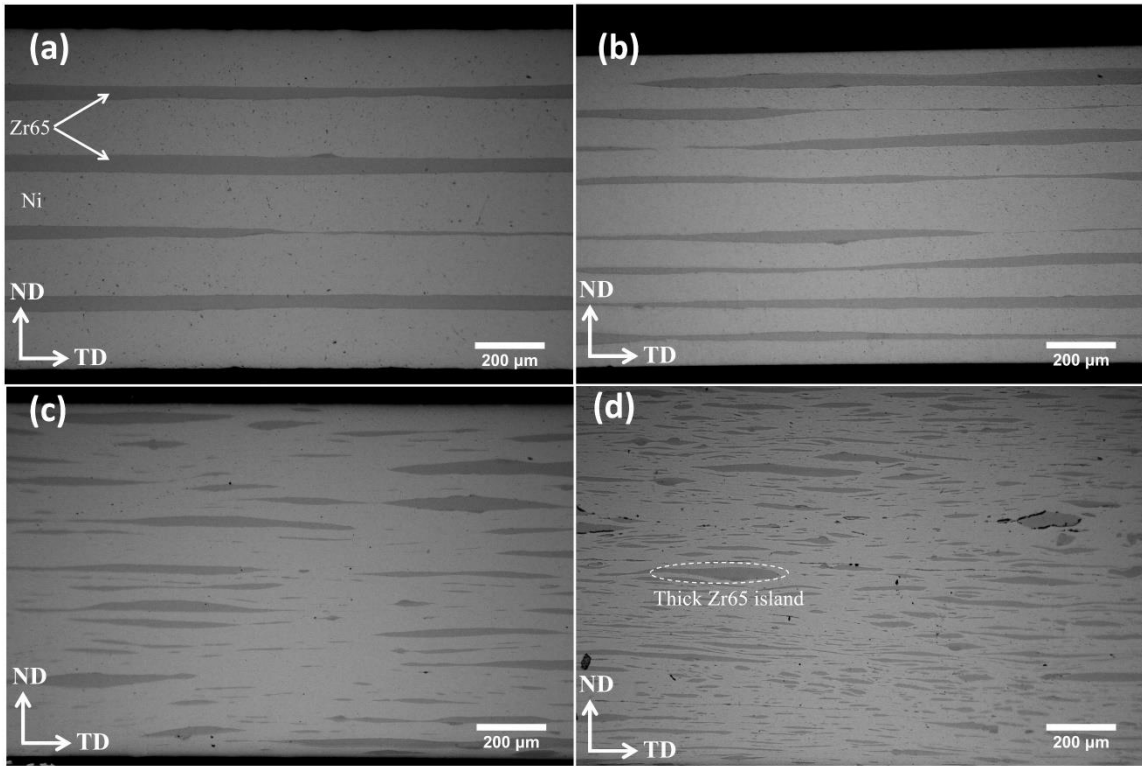
Figure 3.1. Light micrographs of ARB processed Zr65/Ni at different cycles, where darker regions are Zr65 and the brighter regions are Ni. (a) First ARB cycle, (b) second ARB cycle, (c) fourth ARB cycle, and (d) sixth ARB cycle containing a few thick Zr65 islands.

regions of Zr65 appear to have been elongated and discontinuous. In certain regions, the Zr65 phase appears to have gone through minor plastic deformation with a maximum Zr65 thickness of 37 μm (Figure 3.1c). The regions that developed necks during the earlier ARB cycle are stretched thinner during the subsequent rolling cycles. After the sixth ARB cycle, the microstructure contains a combination of thin and thick regions of Zr65 phase with the thickest regions having a maximum cross-sectional thickness of 38

µm; the overall microstructure appears to be more refined compared to the fourth ARB cycle (Figure 3.1d).

The distribution of Zr65 layers and the microstructure of Ni for the ARB-6 sample was investigated via backscatter electron (BSE)-SEM and ion channeling contrast imaging (Figure 3.2). Due to atomic number contrast in BSE imaging, Zr65 appears bright in BSE-SEM micrographs in Figure 3.2a, 3.2b, and 3.2c. Large variation in
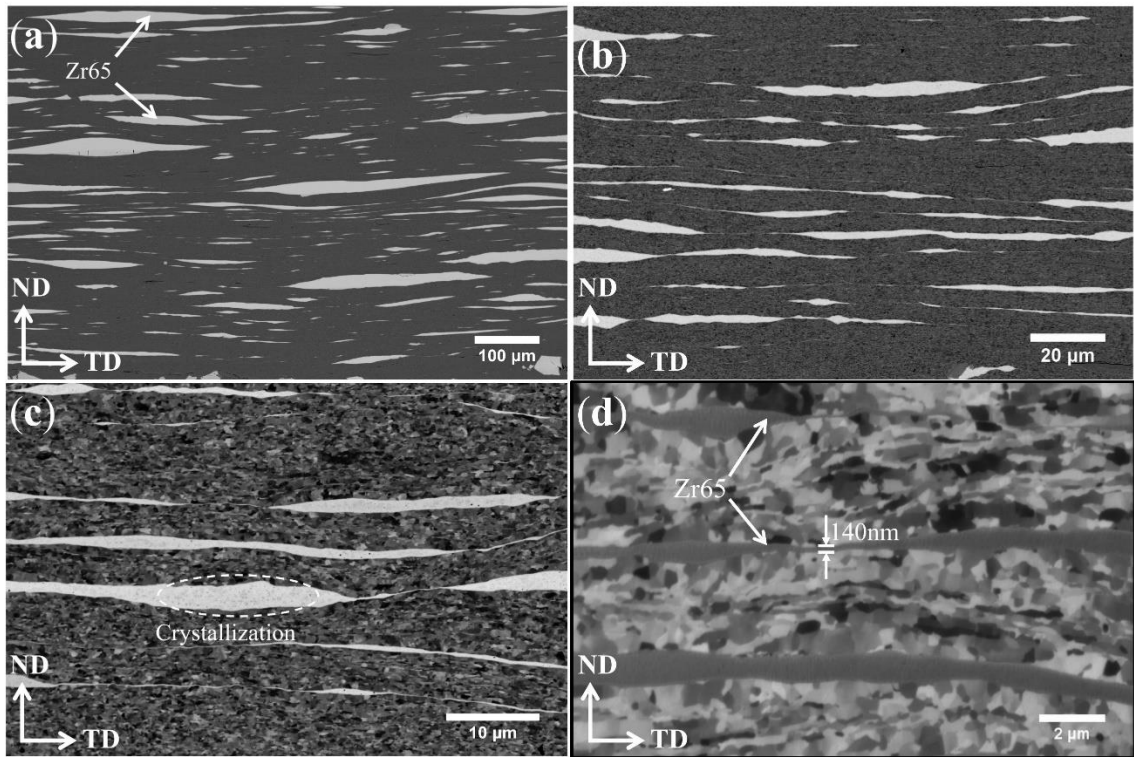
Figure 3.2. BSE-SEM and FIB micrographs of Zr65/Ni after the sixth ARB cycle. (a) Low magnification BSE-SEM micrograph of the Zr65/Ni illustrating Zr65 distribution within the microstructure, (b) higher magnification BSE-SEM micrograph of the composite indicating a large Zr65 thickness variation (c) evidence of Zr65 crystallization in isolated regions, (d) FIB ion channeling contrast micrograph indicating Zr65 thickness as small as 140nm.

thickness of Zr65 can be seen in Figure 3.2a. It appears that during the rolling process a fraction of Zr65 within the microstructure has experienced minimal plastic deformation

while the remaining Zr65 appears to have experienced plastic deformation to a much greater extent, which indicates large flow stress variation of Zr65 and Ni during the rolling process (Figure 3.2a and 3.2b). The Zr65 layers have necking-like features even at higher magnifications, but promisingly, the layers appear to be continuous (Figure 3.2c and 3.2d). Evidence of devitrification of the Zr65 can be seen in Figure 3.2c, which can be distinguished due to electron channeling contrast of BSE signal. Zr65 regions as small as 140nm in thickness can be seen in Figure 3.2d indicates regions that reduced from 60 μm to 140 nm in six ARB cycles. The ion channeling contrast micrograph in Figure 3.2d shows an ultrafine grained (UFG) Ni with grain sizes of approximately 360 nm which was estimated using the mean lineal intercept method.

Since BSE-SEM images denoted potential crystallization of Zr65, the microhardness of the as-received and ARB-processed specimens was compared (Figure
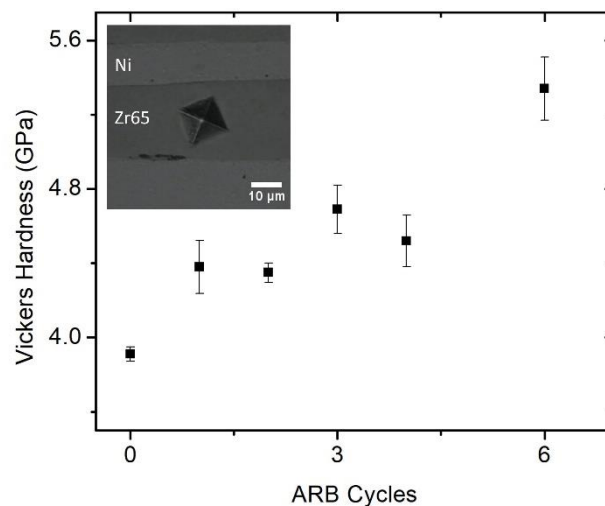

Figure 3.3. Microhardness of Zr65 for as-received and ARB processed samples. For ARB cycles two and beyond, the microhardness values are selectively taken from regions that have gone through minor thickness reduction. The inset shows a typical indentation.

3.3). The abrupt increase in the hardness of Zr65 likely indicates partial crystallization in Zr65 and is further explained in the discussion section. The hardness measurements for the ARB processed samples were taken from the regions that underwent a minimum reduction in thickness and remained in the form of thick islands as seen in Figure 3.1 and 3.2. Upon the first ARB cycle, the average hardness of the Zr65 is seen to increase from 3.91 +/- 0.04 GPa to 4.38 +/- 0.14 GPa. The hardness of these regions is further increased to 4.52 +/- 0.14 GPa after the fourth ARB cycle and then increases up to 5.34 +/- 0.17 GPa after the sixth ARB cycle.

TEM is incorporated to characterize the Zr65/Ni microstructure at higher magnification and to resolve the amorphous/crystalline interface structure (Figure 3.4). The microstructure of Zr65 appears to vary significantly in thickness throughout the microstructure, but individual layers are continuous (Figure 3.4a). An HRTEM micrograph in Figure 3.4c indicates a minimum Zr65 thickness of 34nm within the Ni matrix, and the fast Fourier transform (FFT) indicates that the Zr65 is amorphous in this region (Figure 3.4c). The Zr65/Ni interface region as shown in Figure 3.4d appears to be 3-4 nm in width. The amorphous region is distinguished by a disordered structure, while the crystalline regions are indicated by lattice fringes that are correlated to the atomic planes, which are visible in Figure 3.4d. The transition from crystalline to amorphous is gradual, and some local ordering is observed at the interface (Figure 3.4d).
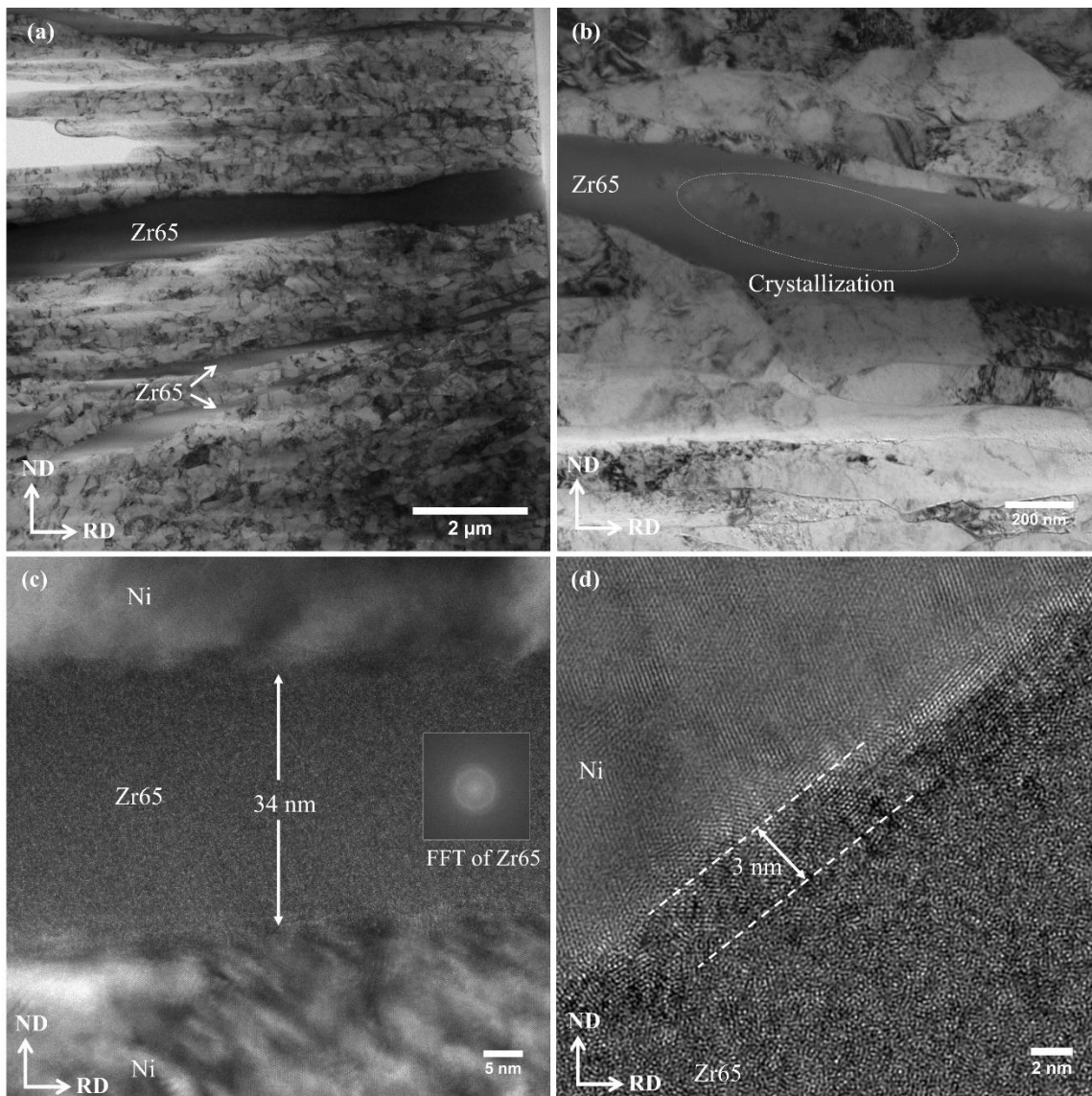
Figure 3.4. TEM micrographs of Zr65/Ni after sixth ARB cycle. (a) Low magnification TEM micrograph indicating large variation in thickness of Zr65 and UFG Ni microstructure, (b) indication of crystallization in Zr65, (c) Zr65 regions as thin as 34nm with respective FFT, (d) Zr65/Ni interface indicating an amorphous/crystalline transition region a few nanometers in width.

3.4 Discussion

Partial crystallization of the Zr65 can increase its flow stress significantly [23], which can alter its plastic flow behavior during the rolling process. To avoid crystallization of Zr65, careful attention must be made regarding the TTT behavior of BMGs. Ideally, the selected BMG must be processed at temperatures close to the lower limit of the T_g to allow longer processing times. According to the TTT diagram of this BMG alloy, the onset of recrystallization at 420 °C will take place in 15 minutes [24]. In this study, the total accumulative time at 420 °C was approximately 12 minutes for six ARB cycles. The partial crystallization that is observed in Figure 3.2c and Figure 3.4b are likely due to overestimation of the TTT behavior. However, other factors such as adiabatic heating can also raise the temperature near T_x and cause partial crystallization.

The hardness increase in the thick Zr65 regions (Figure 3.3) after the first ARB cycle is likely an indication of partial crystallization of Zr65 (hardness was measured from Zr65 regions with large thicknesses). The hardness of a BMG alloy can increase either by partial crystallization when heated above T_g or structural relaxation when heated below T_g [25][23]. In this processing, structural relaxation can be ruled out due to an opposite phenomenon known as rejuvenation that takes place when heating the BMG above its T_g [25]. The hardness of the partially crystallized Zr-based BMGs are known to increase abruptly by an increase in crystallization fraction, and we can see a similar trend in Figure 3.3 [23][26]. This increase in hardness of Zr-based BMGs can be explained by phase mixture model, where the increase in hardness is best described by the rule of mixture of the crystallized and amorphous phases based on their volume fraction and

respective hardness [27]. The hardness of Zr65 is increased from 3.91 +/- 0.04 GPa in the as-received condition to 4.38 +/- 0.14 GPa after the first ARB cycle. This increase in hardness can be correlated to a reduction in deformation of Zr65 in isolated regions. Though some Zr65 regions are partially crystallized and expected to have high flow stresses, further reduction of the Zr65 has taken place up to the fourth ARB cycle. This can be seen by the maximum thickness of Zr65 layers reducing from 52 μm in the first ARB cycle to 37 μm after the fourth ARB cycle with their average hardness of 4.38 +/- 0.14 GPa and 4.52 +/- 0.14 GPa respectively (Figure 3.1 and 3.3). We speculate that during the rolling of partially-crystallized Zr65, the remaining glassy regions flow around the crystallized regions and cause further thickness reduction of the partially-crystallized Zr65 phase. The maximum thickness of Zr65 after the sixth ARB cycle remained identical to the sample processed to fourth ARB cycle. This can be explained by the abrupt increase in hardness of such regions from 4.52 +/-0.14 GPa after the fourth ARB cycle to 5.34 +/- 0.17 GPa after the sixth ARB cycle, which indicates an increase in crystallization fraction of nondeforming regions in the later processing cycles. It is important to note that the hardness increase that we observed in Zr65 layers with an increase in ARB cycles is different from the hardness increase found in ARB processing of crystalline metals [28,29], where the hardness increase in crystalline metals is due to Hall-Petch strengthening.

The ARB process requires the BMG phase to be in the SLR so that the BMG experiences a significant reduction in flow stress at this temperature range (i.e., T_x-T_g) [22]. The flow stress of the BMGs in the SLR is strongly dependent on temperature [22].

It has been shown that a difference of 10 °C in temperature in the SLR can change the flow stress of Zr65 by 125 MPa and significantly influence the flow behavior [22][30]. Therefore, control over temperature is one of the important keys in producing a predictable microstructure. In the implemented experimental setup, precise control over temperature prior to rolling was not possible, and a temperature reduction between 20-40 °C was measured to occur when transferring the sample from the furnace to the rolls within 4-6 seconds. This variation in temperature was dependent on how fast the specimen was placed between the rolls which varied from time to time. Since the temperature of our heated rolls is at least 150 °C cooler than the preheated sample, we expect further cooling of the sample due to conductive heat transfer from the sample to the rollers; however, some of the temperature loss can be recovered by deformation induced adiabatic heating. For an adiabatic deformation, the temperature increase can be estimated by

$$\Delta T = \frac{\sigma_f}{\rho c_p} \ln \left(\frac{1}{1-r} \right) \qquad (1)$$

where σ_f is the average flow stress in Pa, ρ is the density in kg/m^3, c_p is the specific heat in $J/kg°C$, and r is the reduction [31]. For a 45 % reduction, average flow stress of 0.7 GPa, average density of $8.5 \times 10^3 kg/m^3$ and average specific heat of $521 \, J/kg°C$, the adiabatic temperature increase is estimated to be 94 °C. Due to energy dissipation of the sample to the rollers and the ambient we assumed that the temperature of the sample during the rolling process to be within the SLR, but actual temperature could not be

measured with the current experimental setup. A variation in temperature could mean a large difference in the flow stress of Zr65 during each ARB cycle.

During the ARB process, Zr65 layers neck internally during the early ARB cycles (Figure 3.1). The necked regions are greatly stretched with subsequent ARB cycles, while the larger islands experience a minimal reduction in thickness during the later ARB cycles. The shape and size development of Zr65 is likely influenced by the flow stress variation between the Ni and Zr65 as well as local crystallization of the BMG phase. During ARB processing of dissimilar metals with one having more significant flow stress than the other, the stronger metal develops similar necking -like features [32,33]. During the rolling process, the softer metal experiences greater plastic strain compared to the harder metal, which induces a shear frictional force on the hard phase, and the harder phase can experience tensile forces in the rolling direction [33]. The combination of compressive forces in the normal direction from the rolls and the tensile force in the rolling direction causes larger deformation of the harder phase in the necked regions. From the light micrographs in Figure 3.1, it is speculated that during the ARB process, the flow stress of Zr65 was higher than Ni which caused necking of Zr65 layers during the rolling process. Many regions within the composite exhibited layer thickness reductions below 100 nm with some regions exhibiting layers 34 nm in thickness (Figure 3.4). The severe plastic deformation (SPD) has caused the formation of a UFG Ni phase, which will increase the strength of the composite (Figure 3.2b and 3.4a). After each ARB cycle, it is expected that the flow stress of Ni would increase because of SPD-induced grain refinement and work-hardening until reaching a steady-state grain size.

The structure of interfaces plays an important role in the mechanical properties of nanolaminated metals. Unlike crystalline/crystalline interfaces of dissimilar metals which have long-range order of atoms on each side, the BMG on one side of the interface is disordered and demonstrates a lack of long-range order (for regions where the BMG remains amorphous). To accommodate the atomic position mismatch across the a/c interface, certain atomic rearrangements must occur [10]. The Zr65/Ni interface in Figure 3.4c appears to be uneven with a gradual transition from amorphous to crystalline state with an effective interface width of 3-4nm (Figure 3.4d). Molecular dynamics simulations of interface regions between Cu and amorphous Cu/Zr have shown a similar gradual change in disorder with an interface width of 1nm [10]. The large interface width in our specimen suggests prolonged exposure of the material above T_g which allows higher diffusivity of the constituents. This increase in diffusion can facilitate ordering of the Zr65 constituents according to the periodic potential in the Ni lattice; evidence of such ordering can be seen in Figure 3.4d. This gradual change in the atomic order must have potential implications on the mechanical properties of the interface and should be further investigated. It is expected that the chemical composition of the interface region has a direct relation with the atomic ordering observed here and further chemical analysis of the interface is currently underway and will be subject of another publication.

Due to variation in thickness and partial crystallization of the BMG, a combination of different deformation behaviors at room temperature is likely to occur at different length scales of the BMG. An incubation length scale necessary for the propagation of an embryonic shear band is estimated by Shimizu et al. to be

approximately 100 nm for Zr-based BMGs [34]. Below this length scale, sample-size

scale shear localization is prevented, and homogenous plastic deformation via STZ and

embryonic shear bands are predicted to occur. Above this length scale, shear banding will

be the dominant deformation mechanism in the BMG phase. In free standing BMGs,

shear banding have a tendency to initiate at stress concentrators (i.e., surface defects)

[34,35]; however, as discussed by Feng et al., a/c interfaces are preferred sites for

nucleation of shear bands in the BMG which allows large plastic deformation by

activation of multiple shear bands [35]. Given the complex microstructure of Zr65/Ni

composite (Figs. 3.2 and 3.4), one would expect large plastic deformation of the Zr65

phase via multiple shear banding and STZs for thick (>100nm) and thin (<100nm) layers,

respectively. When the BMG phase is deformed via shear bands, the adjacent crystalline

layers will prevent free propagation of the shear bands within the structure. The partial

crystallization of Zr65 (Figure 3.4b), creates additional a/c interfaces that can act as

nucleation sites for multiple shear banding or act as barriers to shear band propagation

that was initiated at the Zr65/Ni interfaces. Experimental evaluation of the mechanical

properties of the composites is currently underway and will be the subject of another

publication.

3.5 Summary

The use of ARB processing technique for the synthesis of a/c nanolaminated

composites has been investigated using a Zr-based BMG with a wide SLR. In order to

performed ARB, the BMG was heated above T_g to sufficiently reduce the flow stress and

allow homogenous deformation. To avoid extensive crystallization during the ARB

process, careful consideration of time constraint imposed by the TTT behavior of the BMG phase is necessary. The a/c interface that resulted from the ARB process has a gradual transition from amorphous to a crystalline structure with an interface width of 3-4nm, and within the interface, local ordering of the BMG phase is observed. Partial crystallization of the BMG phase was observed in some regions within the specimen which also resisted deformation during the rolling process. Regardless of the partial crystallization of the Zr65 phase, most regions appear to be glassy and have reduced in thickness significantly, where some Zr65 regions have obtained thicknesses as low as 34 nm. This indicates that with the optimization of the processing parameters, fabrication of nanolaminates of Zr65/Ni without partial crystallization is highly possible. This process can further be optimized in the future by careful selection of processing parameters and crystalline metal selection.

3.6 References

[1] P.S. Steif, F. Spaepen, J.W. Hutchinson, Strain localization in amorphous metals, Acta Metall. 30 (1982) 447–455. doi:10.1016/0001-6160(82)90225-5.

[2] F. Spaepen, A microscopic mechanism for steady state inhomogeneous flow in metallic glasses, Acta Metall. 25 (1977) 407–415. doi:10.1016/0001-6160(77)90232-2.

[3] W.F. Wu, Y. Li, C.A. Schuh, Strength, plasticity and brittleness of bulk metallic glasses under compression: statistical and geometric effects, Philos. Mag. 88 (2008) 71–89. doi:10.1080/14786430701762619.

[4] F.X. Liu, P.K. Liaw, G.Y. Wang, C.L. Chiang, D.A. Smith, P.D. Rack, J.P. Chu, R.A. Buchanan, Specimen-geometry effects on mechanical behavior of metallic glasses, Intermetallics. 14 (2006) 1014–1018. doi:10.1016/j.intermet.2006.01.043.

[5] C.A. Schuh, A.C. Lund, T.G. Nieh, New regime of homogeneous flow in the deformation map of metallic glasses: elevated temperature nanoindentation experiments and mechanistic modeling, Acta Mater. 52 (2004) 5879–5891. doi:10.1016/j.actamat.2004.09.005.

[6] C.A. Volkert, A. Donohue, F. Spaepen, Effect of sample size on deformation in amorphous metals, J. Appl. Phys. 103 (2008) 083539. doi:10.1063/1.2884584.

[7] D. Jang, J.R. Greer, Transition from a strong-yet-brittle to a stronger-and-ductile state by size reduction of metallic glasses, Nat. Mater. 9 (2010) 215–219. doi:10.1038/nmat2622.

[8] J.-Y. Kim, D. Jang, J.R. Greer, Nanolaminates Utilizing Size-Dependent Homogeneous Plasticity of Metallic Glasses, Adv. Funct. Mater. 21 (2011) 4550–4554. doi:10.1002/adfm.201101164.

[9] Y. Cui, P. Huang, F. Wang, T.J. Lu, K.W. Xu, The hardness and related deformation mechanisms in nanoscale crystalline–amorphous multilayers, Thin Solid Films. 584 (2015) 270–276. doi:10.1016/j.tsf.2015.01.067.

[10] C. Brandl, T.C. Germann, A. Misra, Structure and shear deformation of metallic crystalline–amorphous interfaces, Acta Mater. 61 (2013) 3600–3611. doi:10.1016/j.actamat.2013.02.047.

[11] B. Cheng, J.R. Trelewicz, Design of crystalline-amorphous nanolaminates using deformation mechanism maps, Acta Mater. 153 (2018) 314–326. doi:10.1016/j.actamat.2018.05.006.

[12] Y. Wang, J. Li, A. V. Hamza, T.W. Barbee, Ductile crystalline-amorphous nanolaminates, Proc. Natl. Acad. Sci. 104 (2007) 11155–11160. doi:10.1073/pnas.0702344104.

[13] I.J. Beyerlein, J.R. Mayeur, S. Zheng, N.A. Mara, J. Wang, A. Misra, Emergence of stable interfaces under extreme plastic deformation, Proc. Natl. Acad. Sci. 111 (2014) 4386–4390. doi:10.1073/pnas.1319436111.

[14] L.F. Zeng, R. Gao, Q.F. Fang, X.P. Wang, Z.M. Xie, S. Miao, T. Hao, T. Zhang, High strength and thermal stability of bulk Cu/Ta nanolamellar multilayers fabricated by cross accumulative roll bonding, Acta Mater. 110 (2016) 341–351. doi:10.1016/j.actamat.2016.03.034.

[15] K. Mori, N. Bay, L. Fratini, F. Micari, A.E. Tekkaya, Joining by plastic deformation, CIRP Ann. 62 (2013) 673–694. doi:10.1016/j.cirp.2013.05.004.

[16] N. Bay, Cold Pressure Welding—The Mechanisms Governing Bonding, J. Eng. Ind. 101 (1979) 121. doi:10.1115/1.3439484.

[17] A. Anghelus, M.-N. Avettand-Fènoël, C. Cordier, R. Taillard, Microstructural evolution of aluminium/Al–Ni–Sm glass forming alloy laminates obtained by Controlled Accumulative Roll Bonding, J. Alloys Compd. 631 (2015) 209–218. doi:10.1016/j.jallcom.2014.12.231.

[18] D. East, M.A. Gibson, D. Liang, J.-F. Nie, Production and Mechanical Properties of Roll Bonded Bulk Metallic Glass/Aluminum Laminates, Metall. Mater. Trans. A. 44 (2013) 2010–2020. doi:10.1007/s11661-012-1436-6.

[19] T. Zhang, A. Inoue, T. Masumoto, Amorphous Zr-Al-TM (TM=Co, Ni, Cu) Alloys with Significant Supercooled Liquid Region of Over 100 K, Mater. Trans. JIM. 32 (1991) 1005–1010. doi:10.2320/matertrans1989.32.1005.

[20] W.C. Fan, C.R. Drumm, S.B. Roeske, G.J. Scrivner, Shielding considerations for satellite microelectronics, IEEE Trans. Nucl. Sci. 43 (1996) 2790–2796. doi:10.1109/23.556868.

[21] S.N. Mathaudhu, Fabrication of Amorphous Metal Matrix Composites by Severe Plastic Deformation, Texas A&M University, 2006. http://hdl.handle.net/1969.1/4389.

[22] D. Wang, G. Liao, J. Pan, Z. Tang, P. Peng, L. Liu, T. Shi, Superplastic micro-forming of Zr65Cu17.5Ni10Al7.5 bulk metallic glass with silicon mold using hot embossing technology, J. Alloys Compd. 484 (2009) 118–122. doi:10.1016/j.jallcom.2009.04.092.

[23] Z. Zhang, J. Xie, Influence of relaxation and crystallization on micro-hardness and deformation of bulk metallic glass, Mater. Sci. Eng. A. 407 (2005) 161–166. doi:10.1016/j.msea.2005.07.020.

[24] T. Nagase, Y. Umakoshi, Electron Irradiation Induced Crystallization of the Amorphous Phase in Zr-Cu Based Metallic Glasses with Various Thermal Stability, Mater. Trans. 45 (2004) 13–23. doi:10.2320/matertrans.45.13.

[25]   J. Saida, R. Yamada, M. Wakeda, Recovery of less relaxed state in Zr-Al-Ni-Cu bulk metallic glass annealed above glass transition temperature, Appl. Phys. Lett. 103 (2013) 221910. doi:10.1063/1.4835076.

[26]   U. Ramamurty, S. Jana, Y. Kawamura, K. Chattopadhyay, Hardness and plastic deformation in a bulk metallic glass, Acta Mater. 53 (2005) 705–717. doi:10.1016/j.actamat.2004.10.023.

[27]   H.S. Kim, Strengthening mechanisms of Zr-based devitrified amorphous alloy nanocomposites, Scr. Mater. 48 (2003) 43–49. doi:10.1016/S1359-6462(02)00344-5.

[28]   G. Anne, M.R. Ramesh, H.S. Nayaka, S.B. Arya, Investigation of microstructure and mechanical properties of Mg–Zn/Al multilayered composite developed by accumulative roll bonding, Perspect. Sci. 8 (2016) 104–106. doi:10.1016/j.pisc.2016.04.008.

[29]   S.H.S. Ebrahimi, K. Dehghani, J. Aghazadeh, M.B. Ghasemian, S. Zangeneh, Investigation on microstructure and mechanical properties of Al/Al-Zn-Mg–Cu laminated composite fabricated by accumulative roll bonding (ARB) process, Mater. Sci. Eng. A. 718 (2018) 311–320. doi:10.1016/j.msea.2018.01.130.

[30]   Y. Kawamura, T. Shibata, A. Inoue, T. Masumoto, Deformation behavior of Zr 65 Al 10 Ni 10 Cu 15 glassy alloy with wide supercooled liquid region, Appl. Phys. Lett. 69 (1996) 1208–1210. doi:10.1063/1.117413.

[31]   W.F. Hosford, R.M. Caddell, Metal Forming, Cambridge University Press, Cambridge, 2007. doi:10.1017/CBO9780511811111.

[32]   A. Mozaffari, H. Danesh Manesh, K. Janghorban, Evaluation of mechanical properties and structure of multilayered Al/Ni composites produced by accumulative roll bonding (ARB) process, J. Alloys Compd. 489 (2010) 103–109. doi:10.1016/j.jallcom.2009.09.022.

[33]   H. Yu, A.K. Tieu, C. Lu, X. Liu, A. Godbole, H. Li, C. Kong, Q. Qin, A deformation mechanism of hard metal surrounded by soft metal during roll forming, Sci. Rep. 4 (2015) 5017. doi:10.1038/srep05017.

[34]   F. Shimizu, S. Ogata, J. Li, Yield point of metallic glass, Acta Mater. 54 (2006) 4293–4298. doi:10.1016/j.actamat.2006.05.024.

[35]   S.D. Feng, L. Li, K.C. Chan, L. Qi, L. Zhao, L.M. Wang, R.P. Liu, Control of shear band dynamics in Cu50Zr50 metallic glass by introducing amorphous-crystalline interfaces, J. Alloys Compd. 770 (2019) 896–905. doi:10.1016/j.jallcom.2018.08.192.

Chapter 4: Summary and Future Recommendations

The processing-structure-property relationships in heterogeneously structured metals are investigated. In one work, a gradient of grain size and deformation is produced using the SMAT process. The SMATed Cu revealed a significant increase in the strengths while uniform elongation was significantly reduced. The reduction in uniform elongation was hypothesized to be caused by the reduction in the overall work-hardening rate of the treated specimen. The dislocation-free recrystallized microstructure components can accommodate higher work-hardening rate than the deformed microstructure. The additional work-hardening rate from recrystallized microstructural components can delay the onset of necking during the tension test; therefore, a higher volume fraction of deformation-free-recrystallized microstructural component in S2PD processed metals can increase the overall uniform elongation. Annealing of SMATed Cu at different temperatures permits selective recrystallization of a fraction of the gradient region. A higher volume fraction of the recrystallized region resulted when the SMATed Cu was annealed at higher temperatures, and an increase in the uniform elongation was observed proportionally. A future recommendation would be to measure the work-hardening rate of individual microstructural components in S2PD processed materials to better predict the stress-strain behavior for uniaxial tension tests.

In another work, BMG/Ni (i.e., a/c) composites were fabricated via the ARB process. The a/c interfaces act as stress concentration regions for activation of shear bands. An increase in the overall interface area leads to the activation of multiple shear bands and an increase in plasticity of the BMGs is expected. Utilizing the thermoplastic

formability of BMGs at their SLR, ARB process was performed at T_g of the BMG phase. Initial BMG layers from tens of micrometers were refined to as low as tens of nanometer. A complex amorphous/crystalline interface structure was generated with a gradual transition from a crystalline to an amorphous structure. Partial devitrification of the BMG phase complicated the microstructure and prediction of the mechanical properties; therefore, the ARB processing parameters need to be carefully considered to avoid devitrification of the metallic glass phase. The primary challenge in ARB processing of BMG/metal composites is to achieve temperature control throughout the process. The TTT diagram for the BMG needs to be carefully considered to avoid unwanted devitrification. One future recommendation is to study the role of the crystalline constituent on the work-hardening behavior of the composite. A high work-hardening rate from the crystalline constituent may allow a high uniform elongation during the uniaxial tension test. Given the wide distribution of the layer thicknesses, shear band nucleation at different layer thicknesses can be investigated. Since the a/c interfaces fabricated in this work appear to have unique characteristics, their roles on shear banding need further investigation.